UNIVERSITY OF OKLAHOMA

GRADUATE COLLEGE

# AN ASSESSMENT OF OKLAHOMA WINTER WEATHER THROUGH THE HIGH-RESOLUTION LENS OF UNMANNED AERIAL VEHICLES

A THESIS

SUBMITTED TO THE GRADUATE FACULTY

in partial fulfillment of the requirements for the

Degree of

MASTER OF SCIENCE IN METEOROLOGY

By

DANIEL D. TRIPP
Norman, Oklahoma
2019

AN ASSESSMENT OF OKLAHOMA WINTER WEATHER THROUGH THE HIGH-RESOLUTION LENS OF UNMANNED AERIAL VEHICLES

A THESIS APPROVED FOR THE
SCHOOL OF METEOROLOGY

BY THE COMMITTEE CONSISTING OF

Dr. Elinor Martin, Chair

Dr. Phillip Chilson

Dr. Heather Reeves

## Acknowledgments

First off, I would like to thank Dr. Phil Chilson and the entire team at CASS for supporting the UAV operations. There was a lot of logistical work and engineering support required to collect a dataset in such harsh conditions. Several flights were made in sub-freezing temperatures, all night long, with winds up to 40 mph. For this, I am very thankful for all of the hard work and effort that this team provided to collect such an amazing dataset! In addition to all of their hard work, they have been great friends and colleagues for which I am very thankful.

Secondly, I would like to thank Dr. Elinor Martin and Dr. Heather Reeves for their guidance throughout this project. It was a huge gamble on whether or not we would even capture winter weather in the 2018-2019 season. Seeing as how this opportunity didn't arise till mid February, it has been a quick 8 months and I am very thankful for every dataset, methodology, or critique they have provided to this work. I have grown immensely as a researcher and a meteorologist and much of this has come from my amazing mentors.

Thirdly, several of the graduate student body have been instrumental in my time at OU. Specifically, Brian Greene and Tyler Bell were a huge help in processing UAV data, executing field campaigns, writing code, and teaching me about the world of UAVs and meteorology. I am extremely thankful for Melanie Schroers who has been my coding life-saver, class study partner, and great friend. Everyone from NWC 5700 (Ryan Bunker, Elisa Murillo, Emily Tinney) who have been there from the beginning of this project, kept me laughing, and made work such an enjoyable place to learn and grow through my time at OU.

Last, to all my family and friends in Oklahoma, Arkansas, and Mississippi who have supported me through my journey in school. OU has been such a great opportunity and a blessing which has brought me to meet my best friend Bekah Wheeler.

Without the help of everyone above and so many others not specifically named, this work would not have been possible. Thank you to everyone for pouring into me and supporting me in this endeavor to introduce UAVs into winter weather.

# Table of Contents

**Acknowledgments** **iv**

**List of Tables** **vii**

**List of Figures** **viii**

**Abstract** **xi**

**1 Introduction** **1**
1.1 Motivation/Background . . . . . 1

**2 Data and Methods** **4**
2.1 Storm Reports . . . . . 4
2.2 In-Situ Observations . . . . . 5
2.2.1 UAVs . . . . . 5
2.2.2 Oklahoma Mesonet . . . . . 5
2.3 Models and Reanalysis . . . . . 6
2.3.1 North American Regional Reanalysis . . . . . 6
2.3.2 High Resolution Rapid Refresh Model . . . . . 6

**3 Results** **8**
3.1 Storm Report Climatology . . . . . 8
3.2 Winter Weather Case Study . . . . . 12
3.2.1 Mesoscale Anaylsis . . . . . 12
3.2.2 KAEFS In-Situ Observations . . . . . 19
3.2.2.1 Radiosonde Measurements . . . . . 19
3.2.2.2 UAV Measurements . . . . . 22
3.2.3 Analysis Applications . . . . . 28
3.3 WRF Case Study . . . . . 31

**4 Conclusions** **39**

**Reference List** **42**

## List of Tables

3.1 Summary of melting and refreezing layer thicknesses. Observed data is a combination of radiosonde and UAV measurements. The lowest 50 m are ignored when defining the refreezing layer. . . . . 26

3.2 Design of WRF-ARW numerical weather prediction system for a real data case on February 19th, 2019. Domain locations are laid out in Fig. 3.11 . . 33

## List of Figures

2.1 Idealized temperature profile of an environment near 0°C. The different approaches for finding the geopotential height of the 0°C isotherm discussed in Section 2.3.2 are denoted. . . . . 7

3.1 (A) Winter Storm and (B) Ice Storm reports in Oklahoma from November 1999 - April 2019 by county from the NCEI database. . . . . 9

3.2 NARR average thickness of the surface warm layer (above freezing). . . . . 10

3.3 HRRR analysis of the thickness of the upper level melting layer during the February 19, 2019 winter weather event at KAEFS. Shaded contours are thickness values in meters and the solid blue contour is the surface 0°C isotherm. (A) 12 UTC, (B) 16 UTC, (C) 17 UTC, (D) 20 UTC. . . . . 13

3.4 Oklahoma mesonet 2 meter temperature on February 19, 2019 in °C. The 0°C isotherm is denoted by the lime green line. . . . . 14

3.5 MRMS composite radar reflectivity of the February 19, 2019 case study. This data is not quality controlled in order to visualize the light precipitation that occurred. (A) 16 UTC, (B) 17 UTC, (C) 18 UTC, (D) 19 UTC. . . 15

3.6 HRRR time/height cross section of temperature at KAEFS during the February 19, 2019 winter weather case study. Solid contours denote values above 0°C and dashed contours are values below 0°C. . . . . 16

3.7 Skew-T Log-P diagrams of the radiosonde measurements collected at KAEFS on February 19, 2019. The 0°C isotherm is colored blue, the dendritic growth zone (-12°C to -18°C) is denoted in purple, and the wetbulb temperature is plotted on (A) in light blue. (A) 12:30 UTC, roughly 45 minutes before sunrise. (B) 16:30 UTC, during ice pellet precipitation. (C) 18:30 UTC, during active precipitation. Erroneous wind data removed. (D) 20:30 UTC, conclusion of the event. . . . . 20

3.8 HRRR time (UTC) vs height (m) plot of temperature (top) and dewpoint temperature (bottom) in °C at KAEFS in Washington, OK on February 19th 2019. Mixed winter precipitation began at 16:30 UTC and continued intermittently until 20 UTC. . . . . 24

3.9 UAV time (UTC) vs height (m) plot of temperature (top) and dewpoint temperature (bottom) in °C taken at KAEFS in Washington, OK on February 19th 2019. UAV vertical profiles are denoted by the dashed vertical line with the flight ceiling marked with a star. . . . . 25

3.10 (A) SBC wetbulb temperature profile generated from the 16z HRRR analysis and interpolated to 3 m vertical resolution. (B) SBC wetbulb temperature profile generated from UAV data in the lower levels and the 16z HRRR analysis. Data is interpolated from the UAV flight ceiling to the next analysis level and both datasets have a vertical resolution of 3 m. The surface precipitation type is classified as ice pellet. Classification abbreviations are as follows: RA = Rain, FZRA = Freezing Rain, PL = Ice Pellet, FZDZ = Freezing Drizzle, SN = Snow, or a mixture of these types. . . . . 29

3.11 Domain layout for the WRF-ARW model. The horizontal grid spacing for domains 1 (black), 2 (blue), and 3 (red) are 30 km, 6 km, and 1.2 km. . . . 32

3.12 3 km vertical temperature evolution of the WRF atmosphere simulation of February 9th 2019 at KAEFS. (A) Full temporal and vertical resolution. (B) Re-sampled to hourly analyses and 25 hPa vertical resolution. Precipitation began at 18:15 UTC. Solid contours denote values above 0°C and dashed contours are values below 0°C. . . . . 35
3.13 3 km vertical temperature evolution of the WRF atmosphere simulation of February 9th 2019. Same as Figure 3.12, but for Stratford, OK (55 km southeast of KAEFS). . . . . 36
3.14 3 km vertical temperature evolution of the WRF atmosphere simulation of February 9th 2019 140 km WNW of KAEFS (New Cordell, OK). Precipitation begin at 18:15 UTC. Solid contours denote values above 0°C and dashed contours are values below 0°C. . . . . 38

## Abstract

Winter weather can lead to power grid failures, disruption of transportation, and can impact the local economy. Specifically in the southern Great Plains, short term model analyses struggle to identify the depth and magnitude of melting and refreezing layers associated with winter weather environments. Studies have shown that the temperature and humidity profiles in the lowest 3 km of the atmosphere provide crucial information in determining the precipitation type which aids forecasters in relaying winter weather risks. However, a change as little as 0.5°C in the vertical profile has been found to alter the precipitation type observed at the surface. Therefore, this study employs unmanned aerial vehicles (UAVs) to explore the efficacy of high temporal and vertical measurements in winter weather environments.

A climatology of winter weather storm reports and associated boundary layer characteristics was compiled to gain a spatial understanding of winter weather precipitation types across the state of Oklahoma. The central/southwestern portions of the state are more prone to ice storms, whereas the northern portions of the state typically observe snow. During the 2018-2019 winter season, boundary layer measurements of an Oklahoma winter storm were collected by a UAV and radiosondes for the first time. The High Resolution Rapid Refresh (HRRR) model analyses resolved the melting and refreezing layer thicknesses well, but was 1-2°C warmer than the UAV observations.

Using the spectral-bin classifier algorithm, it was found that UAV measurements can improve discrimination between hydrometer types in environments near 0°C. A WRF modeling study of the same winter weather environment illustrated the growth and decay of melting and refreezing layers on hourly to sub-hourly temporal scales. Additionally, it was found that high horizontal variability can exist in melting and refreezing layers at a distance of 55 km. Therefore, considerations for precise UAV measurements in a statewide network are recommended as a new addition to our current observational network.

# Chapter 1

# Introduction

## 1.1 Motivation/Background

In the Southern Great Plains (SGP), winter weather can have large societal and economic impacts due to heavy ice loading, power outages, travel disruptions, and low predictability of weather systems of this nature (Changnon 2003; Ralph et al. 2005; Call 2010). On average, the SGP (Oklahoma and Texas) observes 1-3 freezing rain days per year and roughly 1-5 snowstorms (accumulating 15.2 cm in 1-2 days) every 10 years (Changnon and Karl 2003; Changnon et al. 2006). Despite the fact that other regions of the U.S. observe more winter weather, it was found that disaster declarations and monetary federal aid for winter weather related disasters is typically highest in the southern U.S. (Changnon 2003; Changnon and Karl 2003; Changnon et al. 2006; Grout et al. 2012). Grout et al. (2012) found that nearly 50% of ice storms in Oklahoma result in a disaster declaration, whereas only around 30% of blizzards or heavy snow storms result in disasters. Meteorologically, this is due to the fact that SGP ice storms are typically associated with long duration icing and abundant moisture (Rauber et al. 2001; Changnon 2003), leaving this geographic region at increased risk for high impact ice storms. Therefore, this study will focus primarily on ice storms and mixed phase precipitation in Oklahoma when referencing winter weather.

Several studies have focused on synoptic patterns and large-scale processes associated with winter weather (Rauber et al. 2001; Mullens et al. 2016). However, it has been shown that smaller-scale processes and boundary layer characteristics are extremely important as they can alter precipitation type (Thériault et al. 2010; Reeves et al. 2014; Stewart et al. 2015). For example, Thériault et al. (2010) showed that a change of as little as 0.5°C in the vertical temperature profile can alter the precipitation type observed at the surface. Additionally, it is common to observe a high degree of horizontal variability in hydrometeor

type in transitional zones from frozen to liquid (environments near 0°C) (Cortinas Jr. et al. 2004; Reeves et al. 2014).

This variability leads to complex situations in which discriminating hydrometeor type becomes one of the leading problems for the winter weather community. Several hydrometeor classification algorithms have been developed and each have their own advantages and biases (Ramer 1993; Baldwin et al. 1994; Bourgouin 2000; Schuur et al. 2012; Reeves et al. 2014, 2016). Reeves et al. (2014) found that algorithms perform well in snow and rain environments (Probability of detection; PODs $\geq 85\%$), but have poor skill at correctly identifying mixed phase precipitation (freezing rain, ice pellets or a mix) with PODs ranging from approximately 30-90%. For example, the Baldwin et al. (1994) algorithm was found to identify ice pellets with a POD of 89.6%, but suffered greatly at detecting freezing rain with a POD of 28.4% (Reeves et al. 2014). Therefore, no one algorithm has proven accurate at forecasting all precipitation types equally.

Another key aspect in identifying precipitation type, is determining the correct horizontal, vertical and temporal scales needed to properly resolve the microphysical and boundary layer processes associated with winter precipitation. Vertically, small fluctuations in wet-bulb temperature are key in determining how much melting or refreezing will occur as a hydrometeor falls through various layers (Thériault et al. 2010; Reeves et al. 2014; Stewart et al. 2015; Reeves et al. 2016). Conversely, increasing horizontal grid spacing in models has been found to have very little impact on precipitation type forecasts on scales up to 50 km (Reeves 2016). With respect to temporal resolution, most ice pellet and freezing rain events typically have durations less than half an hour (Reeves 2016), suggesting that once-hourly analyses of hydrometeor type are not sufficient to produce a meaningful forecast or generate valuable validation statistics.

Despite advancements in numerical weather prediction and algorithm development, forecasting accuracy is still a great challenge in the SGP region (Ikeda et al. 2017; McCray et al. 2019). Previous studies have utilized ground-based and remote-sensed observations

synthesized with numerical weather models, manned aircraft, and radiosondes to gain an understanding of the evolution of the atmosphere. However, studies suggest that despite our current observational network, the lower levels of the atmosphere (specifically the planetary boundary layer (PBL)), are not properly sampled and could provide important details that could improve our scientific understanding of winter weather and forecasting ability (NRC 2009; Moore 2018; Chilson et al. 2019).

Therefore, several researchers have begun implementing unmanned aerial vehicles (UAVs) as a cost-efficient and highly versatile solution to filling the data gaps in the PBL (Houston et al. 2012; de Boer et al. 2016; Koch et al. 2018; Greene et al. 2018; Chilson et al. 2019; Greene et al. 2019; Bell et al. 2019; Segales et al. 2019). The emerging technology of UAVs has proven to become a reliable platform for measuring state variables at fine scales in the atmosphere and is in the beginning stages of being implemented into a statewide 3D mesonet in Oklahoma (Chilson et al. 2019). A warm season study by Moore (2018), demonstrated that assimilating high-resolution low-level data into models can improve forecasts of convective initiation timing and location.

However, cool season precipitation has yet to be studied from the perspective of UAVs. Therefore, this study employs UAVs as a new observational tool to provide new insight into winter weather processes. A climatology of Oklahoma winter weather was utilized for understanding the spatial distribution of precipitation types across the state in addition to the boundary layer characteristics. UAV vertical profiles of active winter precipitation were collected during the 2018-2019 winter season and are compared to the local observational network, as well as model analyses and precipitation type algorithm output. Additionally, this thesis will provide suggestions for UAV applications in winter weather and give insight into how this new technology can be utilized alongside our current observational network.

# Chapter 2

# Data and Methods

## 2.1 Storm Reports

The National Centers for Environmental Information (NCEI) hosts a database of storm reports that was utilized for analyzing impacts to the state of Oklahoma (NOAA/NCEI 2014). A 19 year winter climatology was developed from 1999-2019 to extend Grout et al. (2012). Reports are classified by storm type as Winter Weather, Winter Storm, Ice Storm, Heavy Snow, and Blizzard. Each report is assigned to the county in which it came from and all reports are relayed from the U.S. National Weather Service (NWS or WFO) forecasting offices to NCEI. The state of Oklahoma is serviced by four WFOs and each office has its own unique definition for the five winter weather categories. Ice storm and winter storm were chosen for this study to view differences in spatial impacts for ice and snow. The definitions for each storm type (by WFO) are below and outlined in the National Weather Service Directives (NWS 2019).

1. Ice storm is defined as freezing rain accumulations of 1/4 inch or more at all Oklahoma WFOs.

2. The Amarillo office defines winter storm as snow accumulations of 4 inches in 12 hr or 6 inches in 24 hr.

3. The Norman office defines winter storm as snow accumulations of 4 inches per event.

4. The Tulsa office defines winter storm as snow accumulations of 4 inches in 12 hr or $>$4 inches in 24 hr .

It is noted that different definitions for winter storm will introduce some spatial inconsistencies in the dataset.

## 2.2 In-Situ Observations

### 2.2.1 UAVs

The CopterSonde 2.5 rotary-wing UAV developed by the Center for Autonomous Sensing and Sampling (CASS) at the University of Oklahoma (OU) was utilized for gathering atmospheric data in winter weather. The technical specifications and details regarding atmospheric measurement integrity can be found in other literature (Greene et al. 2018; Barbieri et al. 2019; Greene et al. 2019; Bell et al. 2019; Segales et al. 2019). In general, previous studies conclude that the CopterSonde performs well when compared to other in-situ measurements (temperature and relative humidity), primarily because of intelligent design to ensure sun shielding and appropriate air flow around sensors. However, all previous testing was conducted in fair weather conditions and no other literature, as far as the authors are aware, deals specifically with UAV measurements in winter weather.

### 2.2.2 Oklahoma Mesonet

The Oklahoma Mesonet is comprised of a network of 120 stations that relay weather and soil observations every 5-minutes (Brock et al. 1995; McPherson et al. 2007). There is at least one station in every Oklahoma county measuring temperature, relative humidity, wind, solar radiation, precipitation, and pressure. Post-processed data was collected from the Oklahoma Mesonet's archive and interpolated in between stations at 30 minute intervals for analysis of the surface temperature during the February 19, 2019 winter weather case study.

## 2.3 Models and Reanalysis

### 2.3.1 North American Regional Reanalysis

The North American Regional Reanalysis (NARR) was utilized to build a climatology of storm-related winter weather PBL characteristics (NARR 2005). It has 29 pressure levels with a vertical resolution of 25 hectopascals (hPa) in the lower levels (1000hPa-700hPa) and 50 hPa for the upper portion of the atmosphere. Horizontal grid spacing is 32 km and analyses are produced every 3 hours for the entire North American region.

### 2.3.2 High Resolution Rapid Refresh Model

The High-Resolution Rapid Refresh (HRRR) Model is a cloud-resolving/convection-allowing model with a 3 km grid as well as 3 km radar assimilation (Alexander et al. 2017). Hourly 0-hour analyses from the HRRR (obtained from the archive hosted by the University of Utah (Horel 2018)) were used to obtain a high-resolution depiction of the atmosphere.

The geopotential heights of freezing levels are found using two different methods.

1. The top-down method begins at the highest pressure level and searches down the vertical profile until 0°C is found (Fig. 2.1). Linear interpolation in between levels is used to estimate the exact height (ESRL 2016).

2. The bottom-up method starts at 50 m and searches up the vertical profile for 0°C. The first occurrence where the temperature above the surface crosses the 0°C isotherm is recorded and the exact height is estimated by linearly interpolating between levels (Fig. 2.1). This variable will provide thicknesses of near-surface refreezing levels. If the 50 m temperature is above freezing, no height is recorded.

These two methods usually give the same value, especially in the warm season. However, during the cold season, the difference between these two heights can provide information about melting layers in the lower portion of the atmosphere. Therefore, the difference

between these two heights will be presented hereafter as the ”upper-level melting layer” (i.e. above the surface). In environments where a surface warm layer greater than 50 m exists, more melting will occur counteracting the influence of a refreezing layer. Therefore, these types of environments are filtered out by the algorithm. The authors note that it is possible to have vertical profiles with several crossings of the 0°C isotherm, however, using these algorithms provide a spatial understanding of profiles hovering around 0°C (i.e. possible areas of mixed phase precipitation).

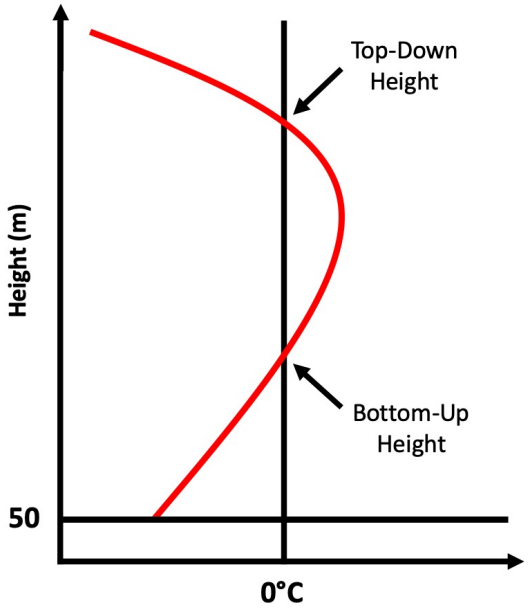


Figure 2.1: Idealized temperature profile of an environment near 0°C. The different approaches for finding the geopotential height of the 0°C isotherm discussed in Section 2.3.2 are denoted.

# Chapter 3

# Results

## 3.1 Storm Report Climatology

The type of winter weather observed in Oklahoma varies widely across the state. In previous studies, ground validation of winter precipitation was primarily augmented by Automated Surface Observing System (ASOS) sites as in Reeves et al. (2014). However, to gain a spatial understanding across a state, a dataset with higher horizontal resolution is required. Therefore, storm reports submitted from individual counties were utilized (Section 2.1) to map the spatial impacts of winter weather.

In Figure 3.1A, winter storm reports are more isolated to the northwestern portion of the state following the same trend found in Grout et al. (2012) and Mullens et al. (2016). By definition, winter storms reports are associated with snow and sleet and were found by Mullens et al. (2016) to commonly be associated with a surface cyclone and a more amplified upper-level flow. Additionally, winter storm reports were found to be concentrated during the months of December, January, and February (hereafter DJF) which also corroborates the findings in other studies (Grout et al. 2012; Mullens et al. 2016).

Ice Storm reports have a distinct pattern with a southwest-northeast oriented belt of frequent frozen precipitation through the central region of the state (Fig 3.1B). This distribution corroborates what has been found in other studies (Grout et al. 2012; Mullens et al. 2016) and denotes an area that, climatologically, observes frozen precipitation approximately once every other year during this study period. Mullens et al. (2016) found that most ice storms are associated with a near surface cold air mass bounded by a warmer air mass to the south. Additionally, southerly warm advection (at 850 hPa) from the Gulf of Mexico is the typical source of moisture for winter weather related events in the SGP.

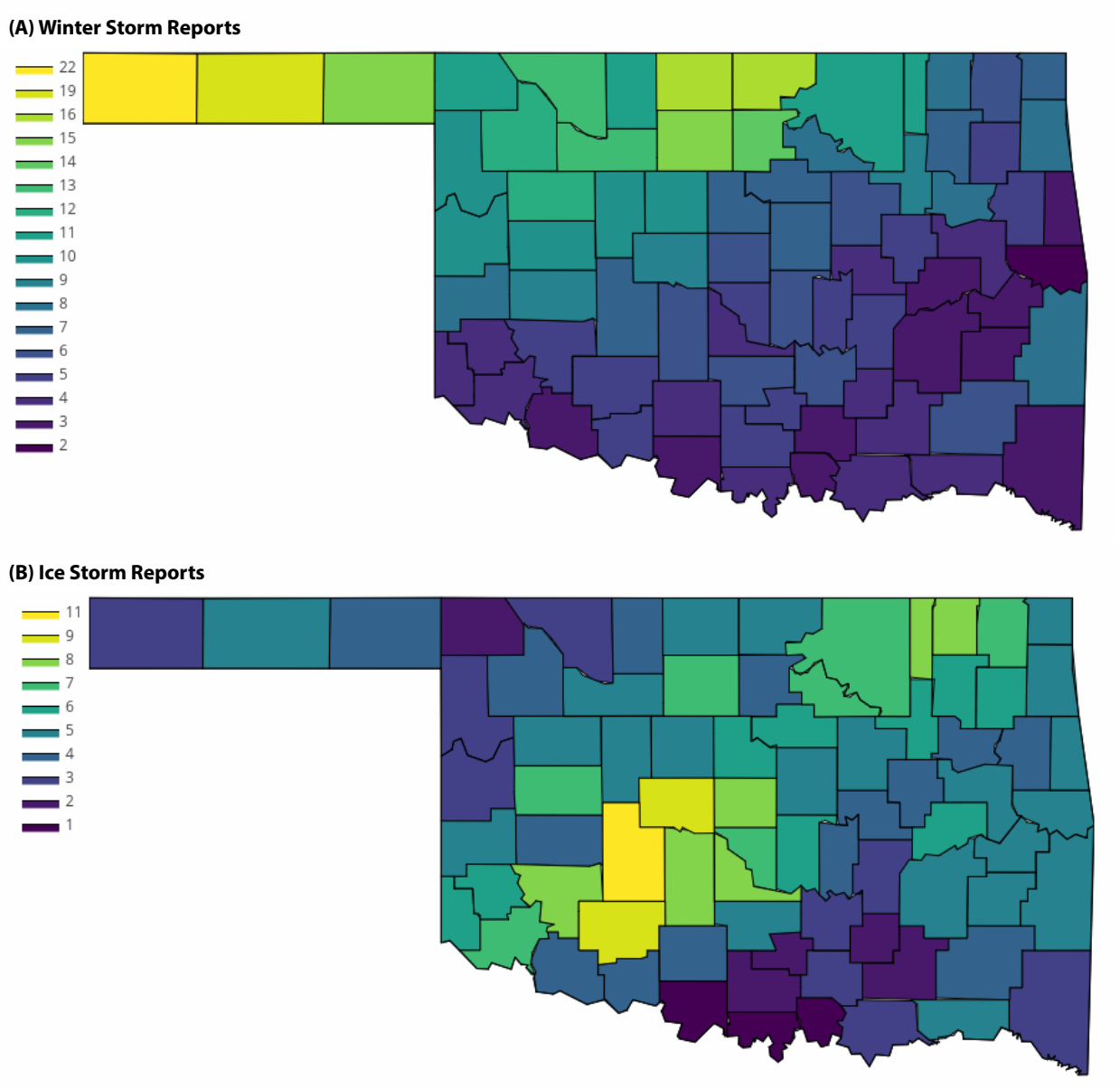


Figure 3.1: (A) Winter Storm and (B) Ice Storm reports in Oklahoma from November 1999 - April 2019 by county from the NCEI database.

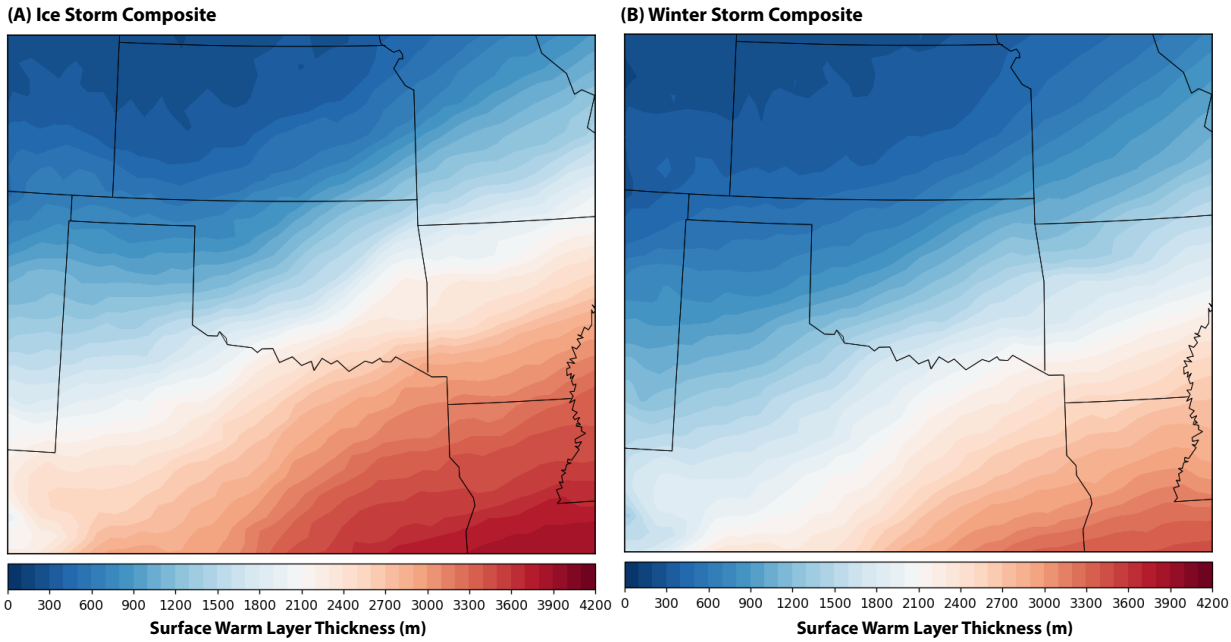


Figure 3.2: NARR average thickness of the surface warm layer (above freezing).

From the spatial distribution of these winter weather events (Fig. 3.1), several precipitation types (snow, freezing rain, ice pellet, or a mix thereof) are possible for a network of UAVs to sample in Oklahoma. To gain an understanding of boundary layer characteristics that occur during ice storm and winter storm events, an event climatology of the last 20 years was built with the NARR. According to Reeves et al. (2014), the lowest 3 km of a temperature profile generally dictate how much melting or refreezing will occur. A similar method to the bottom-up algorithm, outlined in Section 2.3.2 was employed with the NARR. For this algorithm, the surface is assumed to be above freezing and the algorithm searches up the vertical profile to identify the depth of the warm layer at the surface. No interpolation in between analysis levels was used to find the exact freezing height, so the values presented here will likely be an over-estimation. The entire 24-hour period of each storm report was used to determine the average values of the boundary layer characteristics.

Figure 3.2A displays the average near-surface warm layer thickness for ice storm reports from the NCEI. Therefore, since central/southwest Oklahoma (Fig 3.1B) has the

highest concentration of reports, the boundary layer in this region will be the most representative of ice storm environments. A southwest/northeast pattern of 900 to 2100 m thicknesses through central Oklahoma follow the same orientation as the results from Fig 3.1B. Additionally, Figure 3.2A reflects a similar pattern found in Mullens et al. (2016) with warmer air to south and strong baroclinicity across the state. This agrees with other studies (Thériault et al. 2010; Reeves et al. 2014; Stewart et al. 2015) that suggest that freezing rain environments are typically associated with melting layers aloft.

For winter storm reports, Figure 3.1A has the highest concentration of reports in the northwestern portion of the state. This trend aligns with Figure 3.2B which displays a much colder air mass in place in northwestern Oklahoma with surface warm layer thicknesses less than 600 m for this region. Again, these values are a slight over-estimation and encompass the entire 24-hour period surrounding the event. This pattern is representative of snow or ice pellet environments which are typically associated with little or no melting in the vertical profile (Thériault et al. 2010; Reeves et al. 2014; Stewart et al. 2015). Additionally, this pattern represents a much colder air mass that extends to the southern portions of the state with the maximum warm layer thickness just under 2.5 km. This suggests that low-level characteristics that could affect precipitation type in winter storm environments occur much closer to the surface during snow related events.

Overall, this climatology agrees with other studies (Thériault et al. 2010; Reeves et al. 2014; Stewart et al. 2015) that the melting and refreezing layers in winter weather environments lie within the lower 3 km of the atmosphere. Specifically, ice storm environments, climotologically, are associated with greater surface warm layer thicknesses when compared to winter storm environments. Additionally, the horizontal variability of precipitation types in Oklahoma suggests a need for increased observations of vertical profiles spread across the state to capture the unique differences from county to county. Therefore, UAVs are explored in the following sections to illustrate the capabilities and limitations with this technology.

## 3.2 Winter Weather Case Study

### 3.2.1 Mesoscale Anaylsis

During the 2018-2019 winter season, OU CASS deployed the CopterSonde to measure three different winter weather systems in central Oklahoma. Only one of the three deployments captured active precipitation so the forthcoming results will be focused on this event (February 19, 2019). The Kessler Atmospheric and Ecological Field Station (KAEFS; location identified in Fig 3.3), located in Washington, Oklahoma was the base for UAV operations and is a designated OU location where UAVs can fly above the regular flight ceiling laid out by the Federal Aviation Administration (FAA). All UAV flights and radiosonde launches were co-located with the Washington mesonet tower.

To gain an understanding of the horizontal and vertical structure of the atmosphere surrounding KAEFS, the Oklahoma mesonet and the HRRR analyses were utilized. Southerly isentropic lift developed over a cold frontal surface and produced light precipitation throughout a good portion of Oklahoma starting at 16:30 UTC (Fig. 3.5). The southerly warm advection created a melting layer aloft over top of a colder surface refreezing layer. Figure 3.3 depicts the location and thickness of the upper level melting layer throughout the event on February 19th 2019. Areas completely above freezing (beginning 50 m above the surface) are not contoured as considerable melting occurred in these regions resulting in rain. Additionally, environments that were entirely sub-freezing are also not contoured as these environments typically favor snow.

The 0°C isotherm for the HRRR (Fig. 3.3) and the mesonet (Fig. 3.4) indicate a southwest/northeast oriented boundary throughout the event. At 12 UTC (Fig 3.3A) a deep melting layer was in place over the top of a surface refreezing layer in environments hovering around 0°C (Fig. 3.4A ). Northwest of the 0°C isotherm, melting thickness decreased in magnitude as the environment transitioned to complete sub-freezing profiles.

At 16 UTC, the composite reflectivity in (Fig 3.5A) depicts very light precipitation moving into central Oklahoma. However, this was not identified on the lowest radar scans

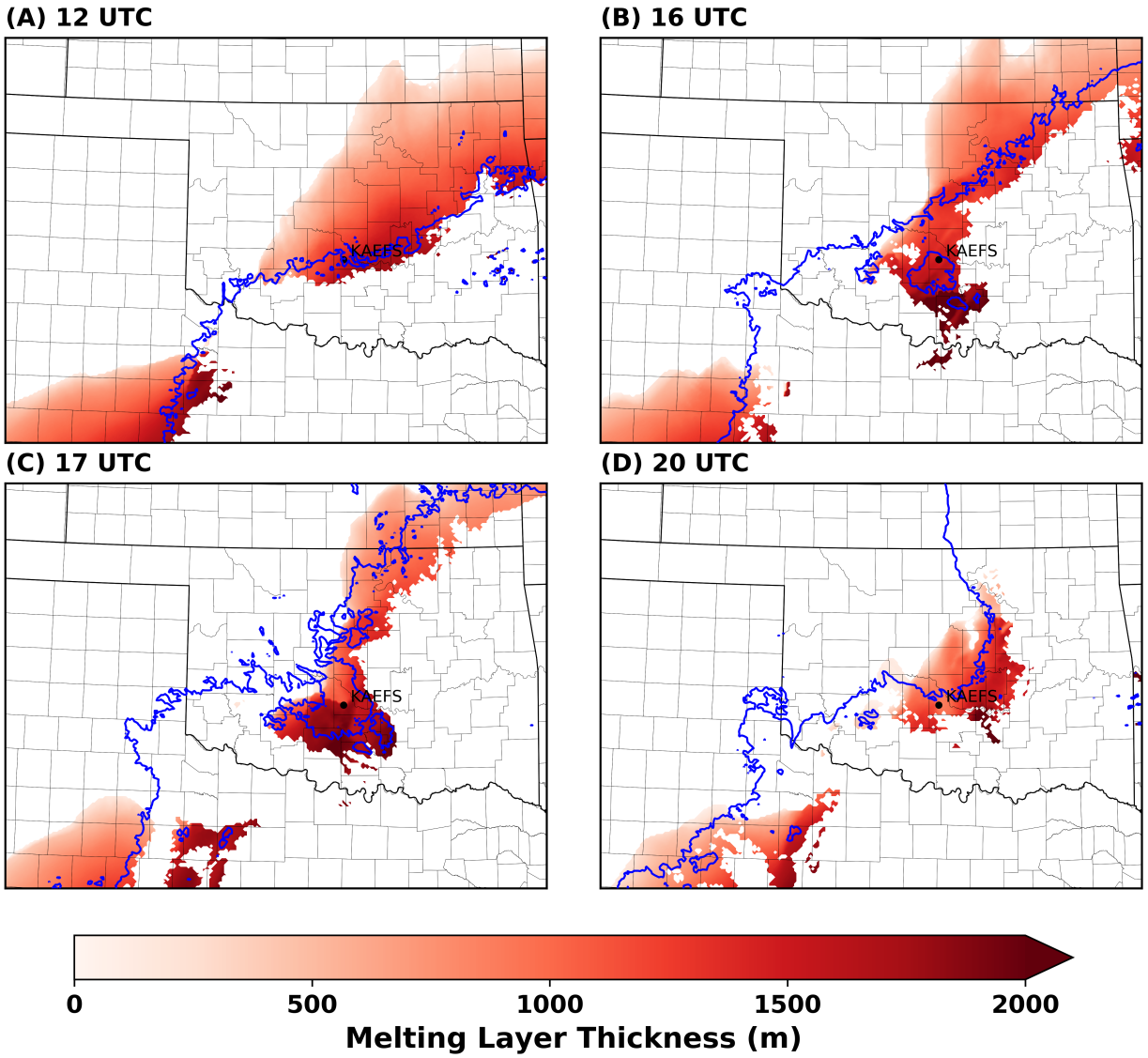


Figure 3.3: HRRR analysis of the thickness of the upper level melting layer during the February 19, 2019 winter weather event at KAEFS. Shaded contours are thickness values in meters and the solid blue contour is the surface 0°C isotherm. (A) 12 UTC, (B) 16 UTC, (C) 17 UTC, (D) 20 UTC.

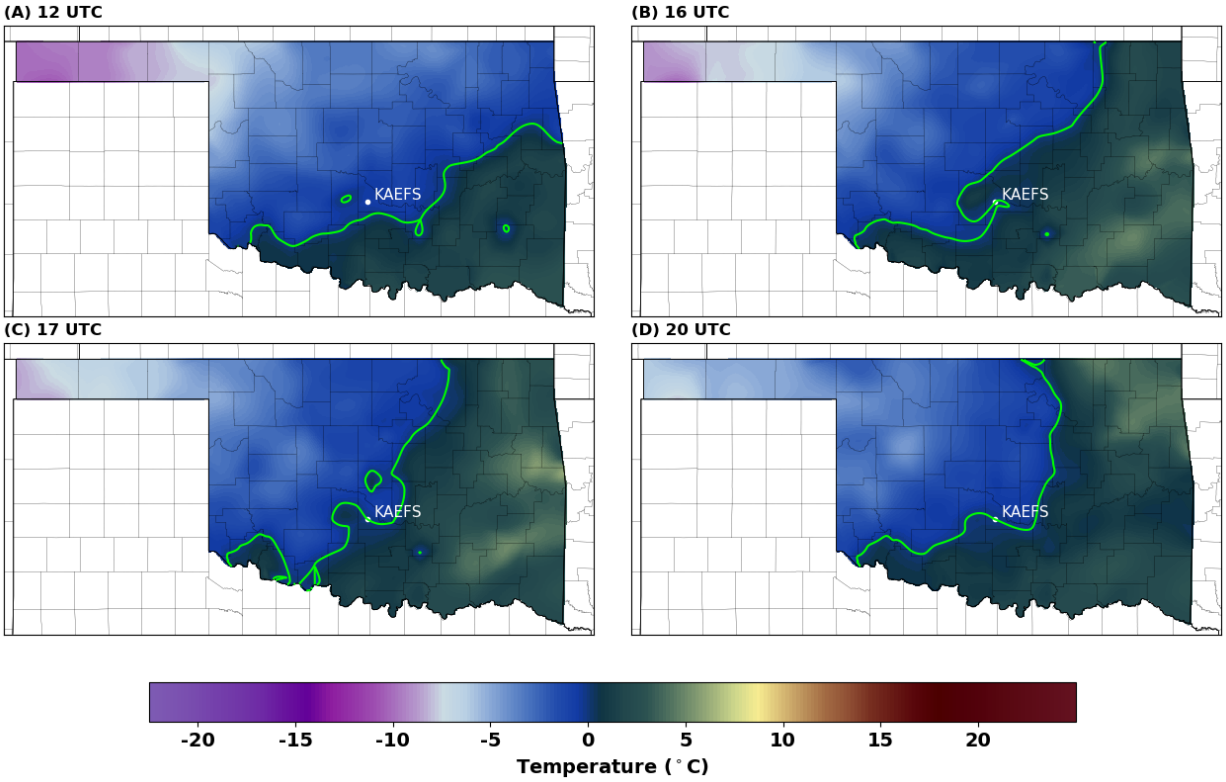


Figure 3.4: Oklahoma mesonet 2 meter temperature on February 19, 2019 in °C. The 0°C isotherm is denoted by the lime green line.

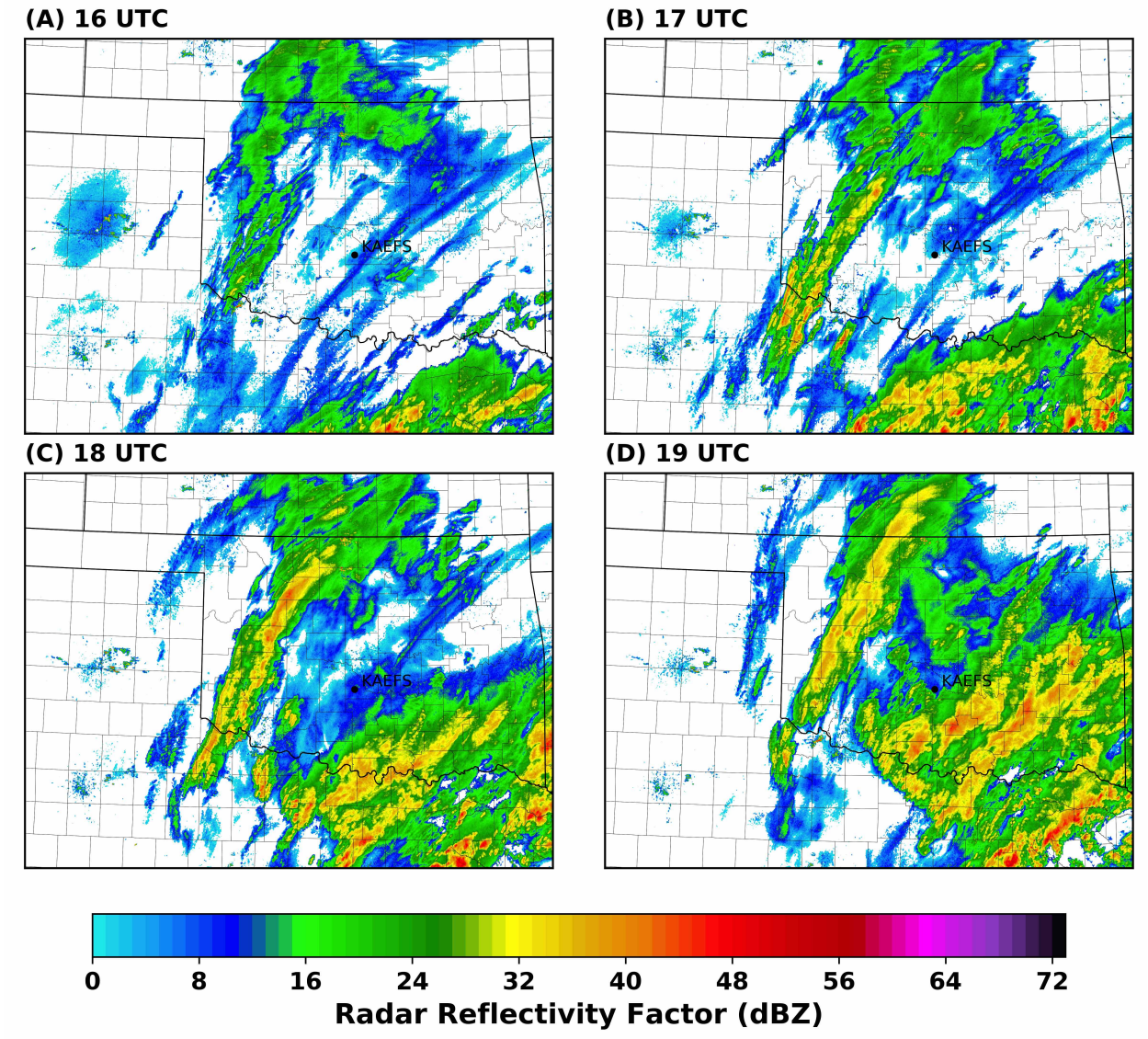


Figure 3.5: MRMS composite radar reflectivity of the February 19, 2019 case study. This data is not quality controlled in order to visualize the light precipitation that occurred. (A) 16 UTC, (B) 17 UTC, (C) 18 UTC, (D) 19 UTC.

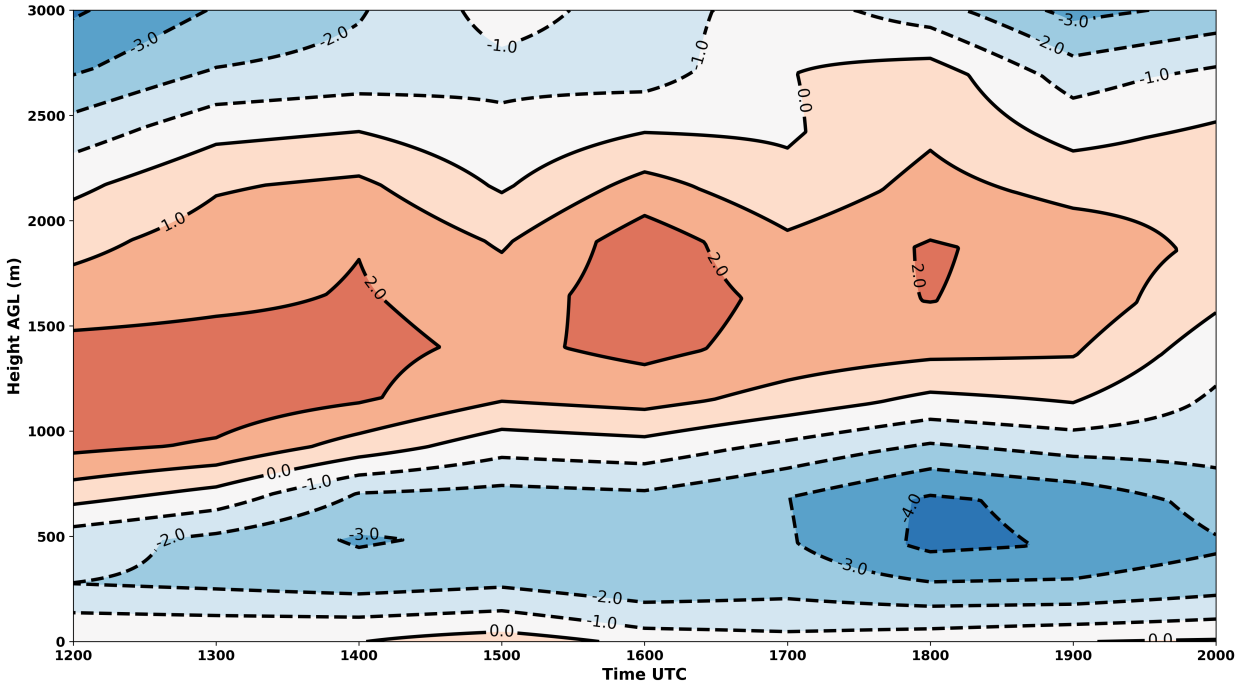


Figure 3.6: HRRR time/height cross section of temperature at KAEFS during the February 19, 2019 winter weather case study. Solid contours denote values above 0°C and dashed contours are values below 0°C.

indicating evaporative cooling occurred in the upper portions of the atmopshere. This led to intensification of the colder air mass near the surface and also increased the thickness of the refreezing layer. For the KAEFS location specifically, the refreezing layer thickness grew from 651 m to 972 m in 4.5 hours (12 UTC to 16 UTC) (Fig 3.6). In terms of temperature, the coldest refreezing layer temperature decreased from -2°C (12 UTC) to -2.8°C (16 UTC). As soon as precipitation reached the PBL at 16:30 UTC, the refreezing layer began to expand in thickness and cool more rapidly due to the evaporative cooling in the layer.

As precipitation formed in central Oklahoma (Fig 3.5 A and B), the surface freezing line advanced farther to the southeast (Fig 3.3C and 3.4C) as wetbulbing, or melting of frozen hydrometeors occurred. However, it should be noted that when comparing the KAEFS two meter temperatures between Fig 3.3C and 3.4C, the HRRR is cooler by 0.5°C when compared to the mesonet. Model uncertainty $>$0.5°C has been found in other studies (Ikeda et al. 2017) and can be attributed to a need for better data assimilation and boundary layer parameterization improvements. The melting layer aloft decreased over KAEFS by 362 m as the onset of precipitation caused this layer to cool by 0.9°C (warmest temperature in layer at 17 UTC = 1.7°C; Fig 3.6) in one hour. The 17 UTC precipitation observed at KAEFS was rain, given that the refreezing layer was not cold enough to refreeze liquid.

Figure 3.3D denotes the time of the conclusion of the field operations as the precipitation began to move out of central Oklahoma. The melting layer reached its minimum thickness at 913 m with the warmest temperature in the layer dropping down to 0.7°C at 20 UTC. The refreezing layer reached a maximum thickness of 1560 m with the coldest temperature at -3.1°C (Fig 3.6; 20 UTC). A dry slot began to work into the upper levels which eroded the precipitation for central Oklahoma around 20:30 UTC. Farther to the northwest, a snow band produced 7.5 inches of snow in Burlington, OK (225 km NW of KAEFS). Areas outside of the snow band observed trace amounts of winter precipitation in central and northwestern Oklahoma.

Overall, the HRRR analyses were able to detect some of the fine scale processes associated with wetbulbing and growth/decay of refreezing/melting layers. Local nuances in surface temperature characteristics were marginally different than the mesonet in some cases; however, these types of errors are commonly observed in numerical weather models. As an analysis tool for this event, the HRRR effectively demonstrated that winter weather processes occur on smaller temporal scales compared to what other numerical weather models or radiosonde networks are able to capture.

### 3.2.2 KAEFS In-Situ Observations

#### 3.2.2.1 Radiosonde Measurements

To further investigate the efficacy of the HRRR model analyses, radiosonde and UAV measurements were taken to capture the evolution of the vertical profile during winter weather. Data collection began before sunrise at 12 UTC with light surface winds and cloudy skies. Winter precipitation moved in at 16:30 UTC in the form of ice pellets (Fig. 3.5). Precipitation type transitioned to all liquid by 17 UTC and continued intermittently until the conclusion of the event at 20:30 UTC. Throughout the entire study period, the surface temperature was around 0°C (±0.5°C; as seen in Fig 3.4) making periods of freezing rain and rain almost indiscernible. No significant icing was observed across the land surface; however, exposed surfaces and objects (antenna equipment, cables, tree branches) had small amounts of ice accretion visible during field operations.

Four iMet radiosondes were launched (12:30, 16:30, 18:30, and 20:30 UTC) sampling every second with an average ascent rate of 3 m $s^{-1}$ in the PBL. The first radiosonde (Fig. 3.7A) was launched 4 hours before precipitation started and captured a pronounced upper level melting layer that is 1578 m thick from 900 hPa to 740 hPa. This agrees with the results discussed in Section 3.2.1 on melting layer depth and indicates a sufficiently cold surface layer in the lower 700 m with the 320 m temp at -3°C. Whereas the general thickness of each layer coincides with the HRRR, there was a 1°C difference in refreezing layer temperature with the radiosonde being colder. The southerly warm advection is evident by the 20 knot wind barbs co-located with the melting layer.

The 16:30 UTC radiosonde (Fig. 3.7B) was released during active ice pellet precipitation. In the lowest kilometer of the atmosphere, evaporative cooling was evident as the 900 hPa temperature cooled to -5.1°C ($\delta$T = 5°C) to the wetbulb temperature and the surface cold layer grew up to 1050 m (860 hPa; melting layer 860-714hPa at 1497 m thick). Again, the melting and refreezing layer thicknesses agree with the HRRR analyses, yet the coldest temperature in the refreezing layer is 2.3°C colder in the radiosonde data. This difference

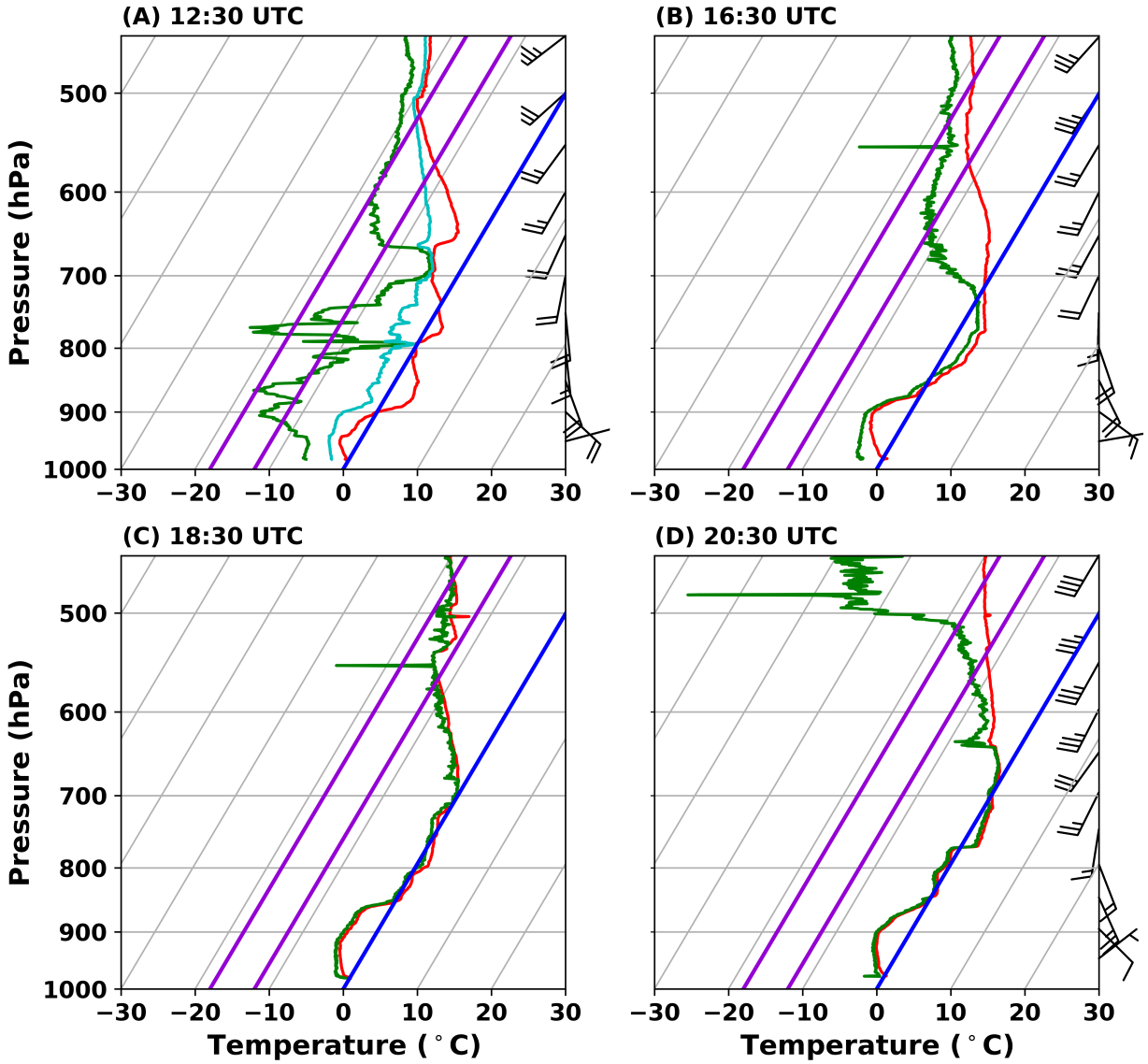


Figure 3.7: Skew-T Log-P diagrams of the radiosonde measurements collected at KAEFS on February 19, 2019. The 0°C isotherm is colored blue, the dendritic growth zone (-12°C to -18°C) is denoted in purple, and the wetbulb temperature is plotted on (A) in light blue. (A) 12:30 UTC, roughly 45 minutes before sunrise. (B) 16:30 UTC, during ice pellet precipitation. (C) 18:30 UTC, during active precipitation. Erroneous wind data removed. (D) 20:30 UTC, conclusion of the event.

in temperature led to the production of ice pellets as the liquid hydrometeors were able to refreeze in this layer. This ice pellet profile agrees with other studies (Thériault et al. 2010; Reeves et al. 2014; Stewart et al. 2015) that suggest that a sufficiently cold layer underneath a melting layer, can lead to a complete refreezing of liquid water producing ice pellets.

The last two soundings (Figure 3.7 C & D) were launched during active precipitation and display a consistent surface cold layer within the lowest kilometer of the atmosphere with a 900 hPa temperature at -4°C (colder than the HRRR by 1°C). However, the melting layer disappears as the sensor package succumbs to the icing conditions. It is apparent in both profiles that a temperature bias to the 0°C isotherm occurs and contaminates the upper portions of the data collected. This issue is discussed in Waugh and Schuur (2018) who found that the sensor itself can become encapsulated in ice, which can lead to an under-representation of the upper level warm layer and can cause other measurement errors. In addition to a temperature bias in Figure 3.7C, erroneous 105 knot low-level winds were contained in this data and therefore removed from the profile.

The radiosonde data further corroborates the HRRR analyses on melting and refreezing layer depth. However, the low-level temperature profile was found to be cooler by 1-2°C in the radiosonde dataset. These differences are very important when resolving how much melting or refreezing will occur in a given profile.

#### 3.2.2.2 UAV Measurements

It is evident that there are differences between the HRRR model analyses and the observations that can impact the precipitation type in environments near 0°C. Radiosondes, specifically, can capture in-situ observations in the upper parts of the atmosphere where no other observations are routinely taken. However, there are a few caveats associated with radiosonde measurements.

1. Seidel et al. (2011) found that the average radiosonde drift in the lower troposphere is 5 km. Therefore, these measurements are considered quasi-vertical profiles. However, a quasi-vertical profile may not be appropriate when dealing with winter weather environments involving high horizontal variability.

2. Radiosondes typically ascend too rapidly in the lower atmosphere to be able to ascertain precise measurements of the PBL (NRC 2009). Slower ascent rates are utilized in field campaigns, but measuring at high temporal frequencies can be very costly as the instrumentation is typically not recoverable.

3. Our current radiosonde network for the state of Oklahoma consists of two balloon launches a day at one location. Therefore, measurements on this horizontal and temporal scale are not able to accurately represent small-scale processes associated with winter weather.

Therefore, UAVs were employed for this event to gain a high temporal and vertical resolution of the winter weather environment at KAEFS. The UAV was programmed to ascend vertically at 3 m $s^{-1}$ and obtain temperature and relative humidity measurements every second up to a maximum flight ceiling of 1500 m. Vertical profiles were gathered from 12 UTC through 20 UTC with a total of 18 flights at 15-30 minute intervals on average. As flights in active winter precipitation had never been tested on this aircraft, the temporal resolution varied throughout the study period as weather conditions (primarily icing) could

affect flight performance. Additionally, the flight ceiling was adjusted throughout the study because of icing, high winds, and visibility constraints laid out by the FAA.

The UAV temperature measurements agree within $\pm 0.5^{\circ}$C with the mesonet tower and within $\pm 1^{\circ}$C with the radiosonde data. A similar comparison study has been done by Greene et al. (2019) and Bell et al. (2019) in non-precipitating environments and found better agreement between measurements. One primary constraint with radiosonde comparisons is that the balloon must clear the airspace before the UAV can ascend. Therefore, two of the balloon launches were spaced by about 15-20 minutes from the UAV flights in active precipitation. This led to some spread between the two datasets. However, because mixed phase winter precipitation occurs on short temporal scales (Reeves 2016), and the evaporative cooling discussed in Section 3.2.2.1 is evidence of a rapidly changing environment, the spread in measurements is likely representative of the Washington, OK environment. Additionally, the greatest spread in the 12:30 UTC comparison (non-precipitating) was $\pm 0.5^{\circ}$C which infers good agreement between these datasets.

Figure 3.8 is a time-height cross section of HRRR temperature and dewpoint data corresponding to the UAV flights. Figure 3.9 is a UAV cross section of the temperature and dewpoint temperature in the PBL from dawn to the end of the winter precipitation. Each UAV vertical profile is denoted by a dashed line and the flight ceiling is marked with a star. Any features in between the dashed lines (specifically, small temperature inversions) are a product of the interpolation scheme and may not always be representative of the environment. A few things to note from this dataset:

1. At 12 UTC, from 645 m down to the surface, a refreezing layer is present as in previous datasets. The base of the upper level melting layer (also seen in Fig 3.8 & 3.7) began around 645 m and was very dry with a dewpoint depression of roughly 13$^{\circ}$C. Because of the southerly warm air advection associated with higher winds (20-25 knots), the flight ceiling was limited to just under 800 m.

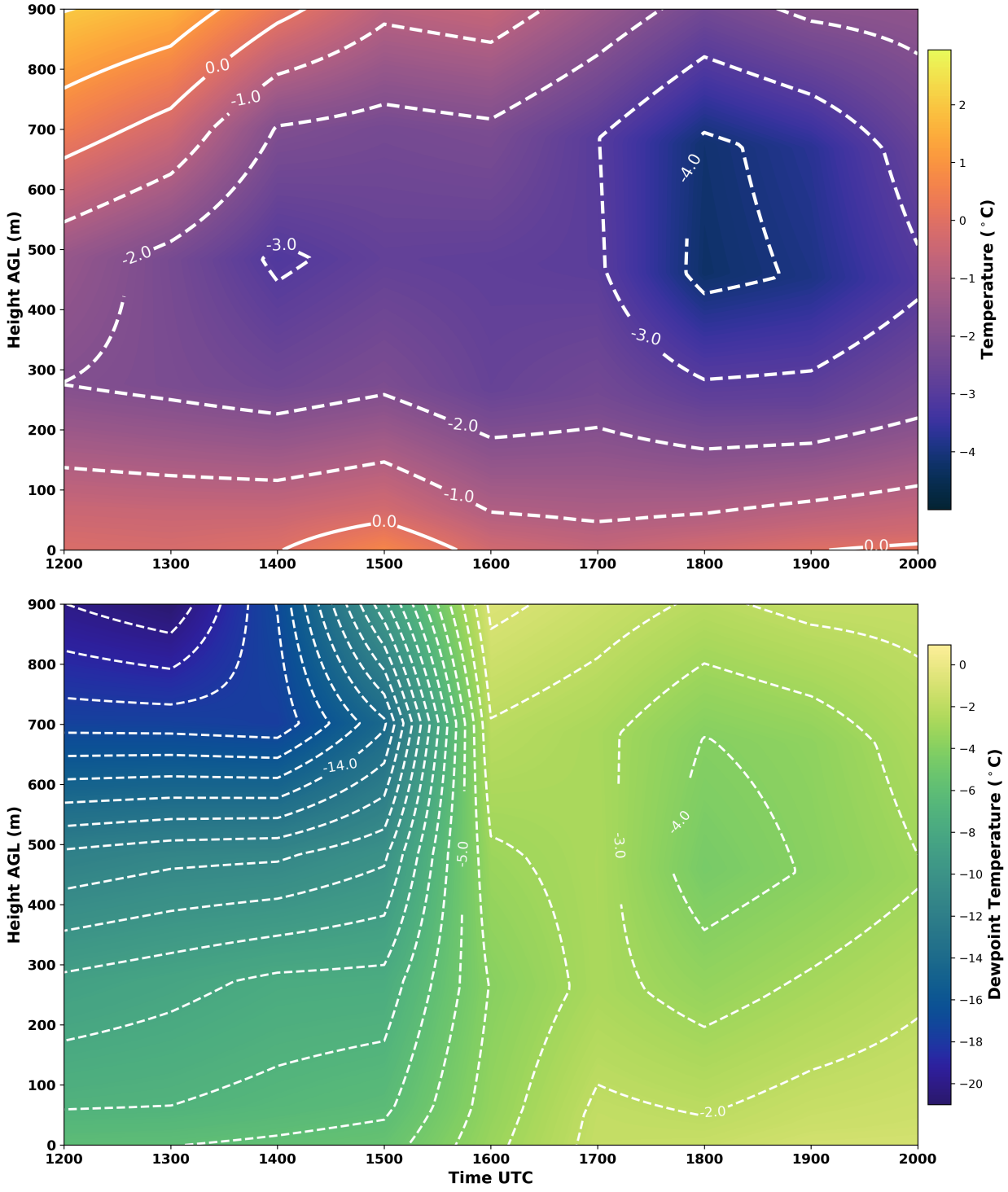


Figure 3.8: HRRR time (UTC) vs height (m) plot of temperature (top) and dewpoint temperature (bottom) in °C at KAEFS in Washington, OK on February 19th 2019. Mixed winter precipitation began at 16:30 UTC and continued intermittently until 20 UTC.

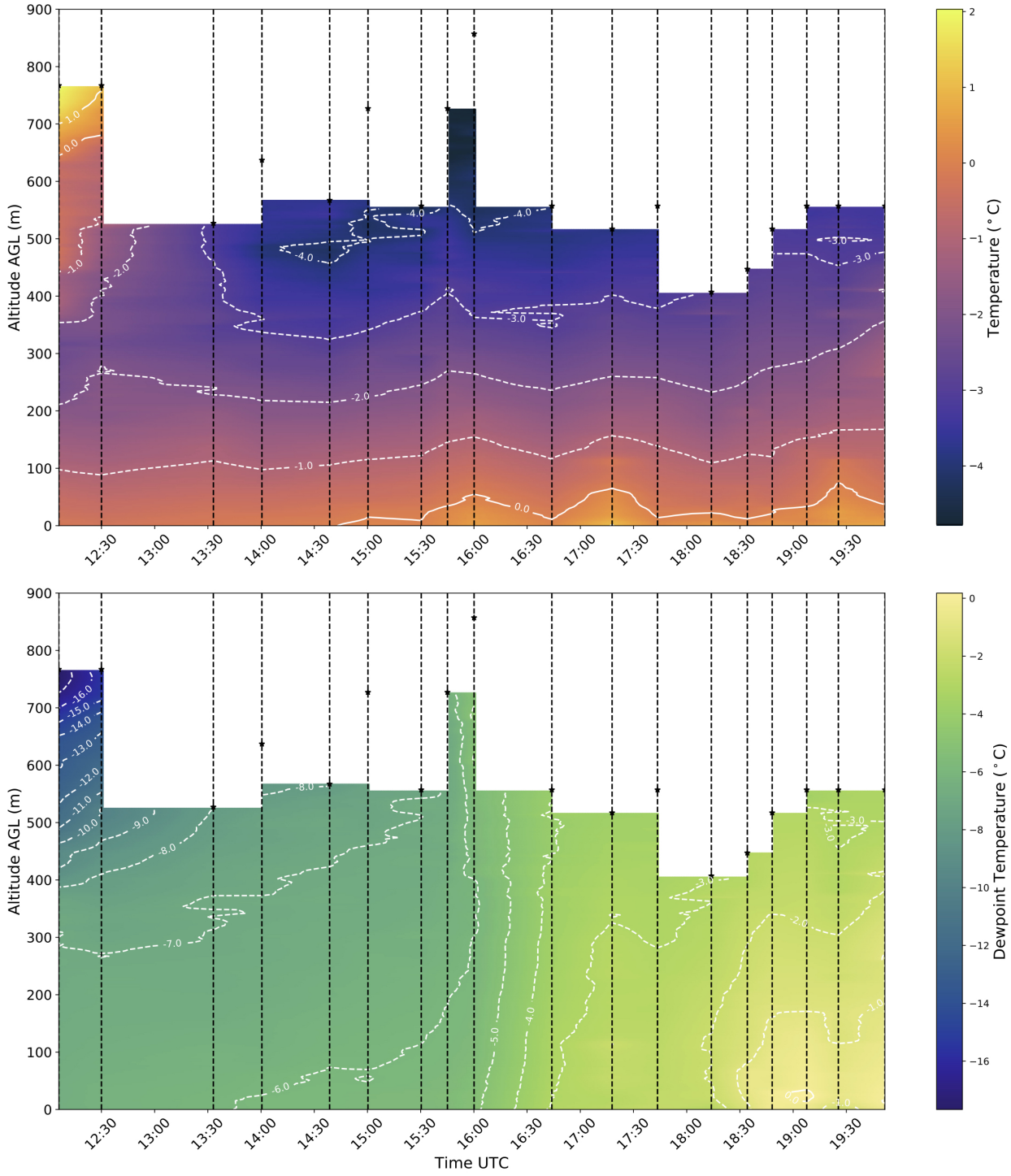


Figure 3.9: UAV time (UTC) vs height (m) plot of temperature (top) and dewpoint temperature (bottom) in °C taken at KAEFS in Washington, OK on February 19th 2019. UAV vertical profiles are denoted by the dashed vertical line with the flight ceiling marked with a star.

2. At 520 m, evaporative cooling dropped the temperature from -1°C (12 UTC) to -4°C at 16:30 UTC (beginning of ice pellet precipitation). The UAV data aligns with the radiosonde observations and displays a colder refreezing layer (Section 3.2.2.1). The onset of precipitation is also denoted in Figure 3.9 by the isodrosotherms turning vertical.

3. Approximately 1.5 hours after sunrise (14:40 UTC), the lower 25-50 m of the atmosphere rose above 0°C and hovered around the freezing point for the rest of the study period. Each time the 0°C isotherm dips back down to the surface (after 16:30 UTC) coincides with active precipitation in the area.

Table 3.1: Summary of melting and refreezing layer thicknesses. Observed data is a combination of radiosonde and UAV measurements. The lowest 50 m are ignored when defining the refreezing layer.

| | **HRRR Melt Layer** | **Observed Melt Layer** | **HRRR Refreezing Layer** | **Observed Refreezing Layer** | **Observed Precipitation** |
|---|---|---|---|---|---|
| **12:00 UTC** | 1462 m | | 651 m | 645 m | |
| **12:30 UTC** | | 1578 m | | 650 m | |
| **16:00 UTC** | 1471 m | | 972 m | >850 m | |
| **16:30 UTC** | | 1497 m | | 1050 m | Ice Pellets |
| **17:00 UTC** | 1109 m | | 1074 m | >500 m | Rain |
| **18:30 UTC** | | N/A | | 1119 m | Rain |
| **19:00 UTC** | 1149 m | | 1134 m | >500 m | Rain/Drizzle |
| **20:00 UTC** | 913 m | | 1560 m | >520 m | Rain/Drizzle |
| **20:30 UTC** | | N/A | | 1011 m | |

The in-situ observations in Figures 3.7 and 3.9 display complementary evidence of a refreezing layer around a kilometer thick, leading to the production of ice pellets at 16:30 UTC. Additionally, a low-level warm pocket at the surface was identified which kept ice accumulations almost non-existent for this location. The results match very closely with

the observed radiosonde profiles discussed in Section 3.2.2.1. The primary difference is that the UAV was able to capture the evolution of the PBL on much higher temporal scales than the HRRR or radiosondes. From an observational standpoint, no other instrumentation network is able to capture in-situ observations at this temporal resolution. Table 3.1 provides a summary of the melting/refreezing layer thicknesses from each of the different datasets. This illustrates that real-time in-situ observations from UAVs, on hourly to sub-hourly temporal scales, could add valuable information about the vertical structure of the atmosphere for winter weather analyses.

### 3.2.3 Analysis Applications

Considering the 3D mesonet concept discussed in Chilson et al. (2019), there is a need to determine whether the differences between model analyses and observations impact precipitation classification algorithms. To illustrate the impact at a fixed location, the spectral-bin classifier (SBC) was chosen as a tool to compare model analysis to a hypothetical UAV/model hybrid analysis. The SBC is a precipitation type algorithm that calculates the liquid-water fraction of hydrometeors across a given drop-size distribution (DSD) to determine the surface precipitation type (Reeves et al. 2016). The algorithm is able to diagnose six different categories of precipitation (rain, snow, rain-snow mix, freezing rain, ice pellet, and a freezing rain-ice pellet mix) by analyzing a given temperature and relative humidity profile. Compared to the algorithms discussed in Section 1.1, the SBC demonstrates higher skill at correctly identifying freezing rain and ice pellets with PODs for these precipitation types around 63% (Reeves et al. 2016). Again, other algorithms may have higher POD scores for one precipitation type, but none of them perform this well for both freezing rain and ice pellets.

Reeves et al. (2016) denotes the SBC is sensitive to the ice nucleation temperature, the degree of riming above a melting layer, and the drop size distribution. Utilizing the ice nucleation temperature of -6°C did not provide the correct precipitation type for any dataset (Coldest Temperature: HRRR = -2.8°C, UAV & Radiosonde = -5°C). Therefore, the ice nucleation temperature was increased to -5°C for both profiles to force at least one of the datasets to align with the observed ice pellet precipitation which occurred 30 minutes later.

A variety of hybrid UAV/model vertical profiles were tested with the SBC to explore the differences in algorithm output when compared to pure model analyses. Figure 3.10A shows the vertical wetbulb temperature profile with the associated hydrometeor type for the 16z HRRR analysis. The melting layer in the HRRR produces a complete melt of all

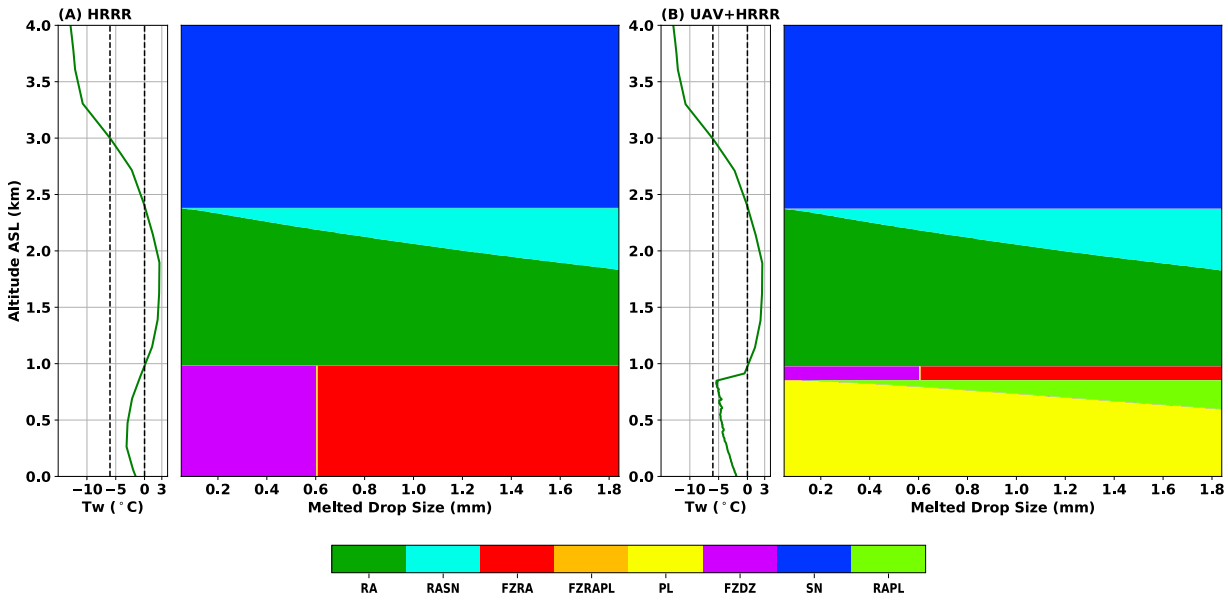


Figure 3.10: (A) SBC wetbulb temperature profile generated from the 16z HRRR analysis and interpolated to 3 m vertical resolution. (B) SBC wetbulb temperature profile generated from UAV data in the lower levels and the 16z HRRR analysis. Data is interpolated from the UAV flight ceiling to the next analysis level and both datasets have a vertical resolution of 3 m. The surface precipitation type is classified as ice pellet. Classification abbreviations are as follows: RA = Rain, FZRA = Freezing Rain, PL = Ice Pellet, FZDZ = Freezing Drizzle, SN = Snow, or a mixture of these types.

hydrometeors down to 1 km before the wetbulb temperature drops below freezing, resulting in a freezing rain classification for droplets larger than 0.6 mm and freezing drizzle for smaller droplets. Figure 3.10B incorporates the same 16z HRRR vertical profile, except the lower levels of the profile are populated by the UAV data and interpolated from the flight ceiling to the closest analysis level. The resulting surface precipitation type when incorporating the UAV data changes to ice pellet which corroborates what was observed 30 minutes later at KAEFS. The UAV flight ceiling in Fig 3.10B is 857 m, and is associated with a rapid shift towards the 0°C wetbulb temperature as the interpolation from the UAV to the HRRR moves from -5°C to 0°C in less than 100 meters. A similar analysis was conducted with the 16:30 UTC radiosonde and yielded almost identical results to that presented in Figure 3.10B. Despite the fact that none of the data produced the correct output for the -6°C ice nucleation temperature suggested by Reeves et al. (2016), this highlights the ability of UAVs and radiosondes to more accurately represent the PBL refreezing layer in comparison to the HRRR analysis.

## 3.3 WRF Case Study

Each scenario of melting and refreezing is unique and can be a complex situation to resolve within models. However, it has been shown here that high-temporal analyses of winter systems from UAVs can provide a clearer picture of the evolution of the atmosphere. Therefore, the WRF-ARW (Weather Research and Forecasting-Advanced Research WRF) model was utilized to simulate a real-data case study of the February 19th 2019 winter weather event.

The WRF model version 4.1 (Skamarock et al. 2019) is a mesoscale numerical weather prediction system that can be utilized to simulate atmospheric phenomena at various temporal and spatial scales. The WRF simulation for this study consisted of 3 domains scaling from 30 km to a 1.2 km grid spacing outlined in Figure 3.11 and Table 3.2. Two-way nesting was employed so the smaller domains fed fine scale data back into the surrounding larger domain calculations. Each domain was run with 80 vertical levels from the surface to 100 hPa. Cumulus convection was parameterized for the largest domain, but was explicitly resolved for the 6 km and 1.2 km domains. All other parameterizations were chosen to closely mirror the HRRR model since the analysis data discussed in Section 3.2.1 resolved most of the features correctly. To avoid an explicit duplication of the HRRR, the NARR was chosen for the initial and boundary conditions. The WRF raw output was processed by the Unified Post Processor (UPP 2019) to obtain the same freezing level variables utilized by the HRRR as outlined in Section 2.3.2.

The smallest 1.2 km domain output data at 15 minute intervals to simulate a similar temporal resolution to the UAV data. Average spacing between model levels in the lower troposphere was 112 m (e.g. $\delta z = 112$ m). Therefore, data was linearly interpolated to the 3 m UAV resolution when calculating melting/refreezing levels. Generally, the WRF model was able to recreate the precipitation associated with the event; however, there were some differences in the temperature profile and timing of the event (Fig. 3.12A).

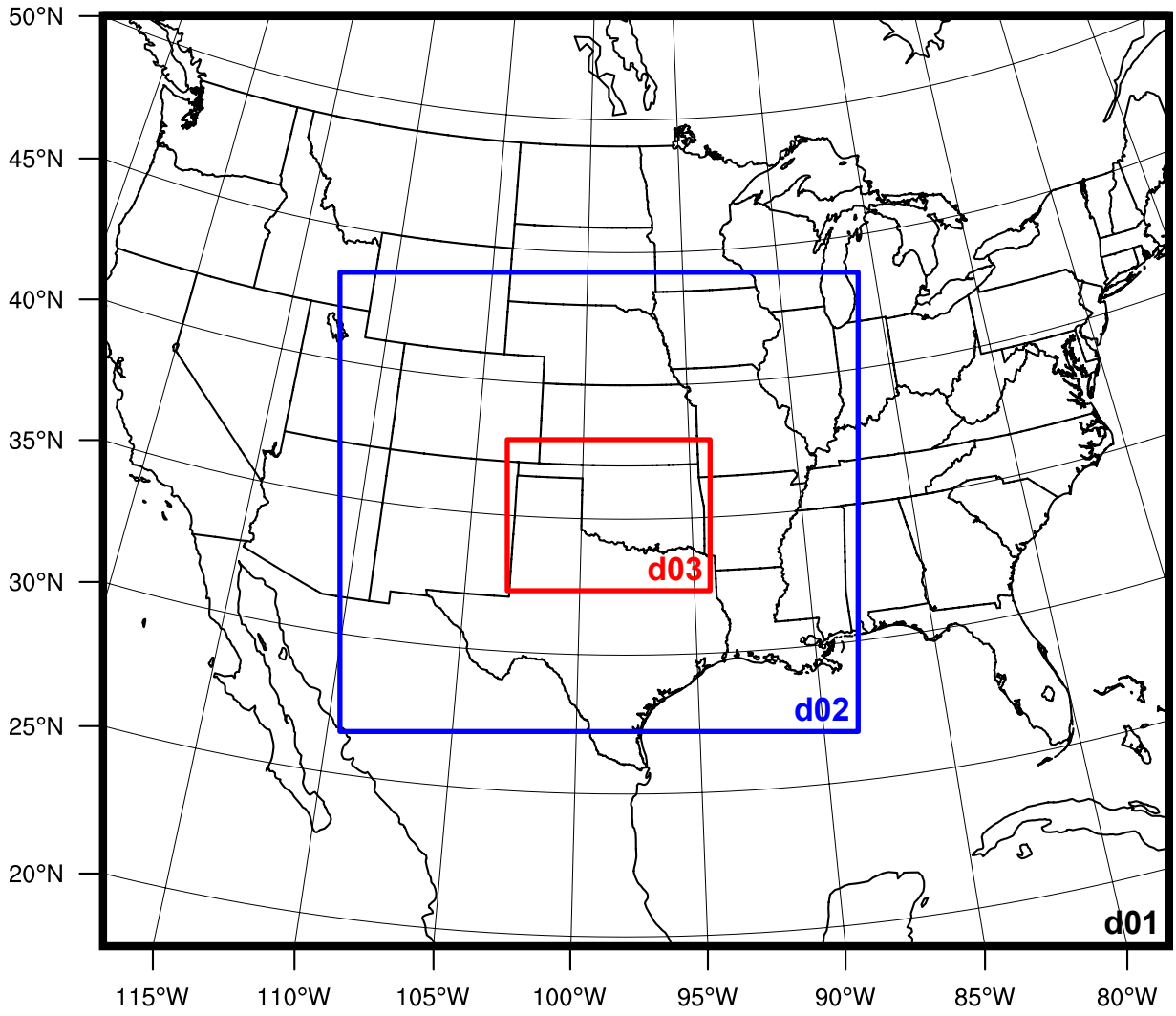


Figure 3.11: Domain layout for the WRF-ARW model. The horizontal grid spacing for domains 1 (black), 2 (blue), and 3 (red) are 30 km, 6 km, and 1.2 km.

Table 3.2: Design of WRF-ARW numerical weather prediction system for a real data case on February 19th, 2019. Domain locations are laid out in Fig. 3.11

| **Model Settings** | **Domain 1** | **Domain 2** | **Domain 3** |
|---|---|---|---|
| Horizontal Grid Spacing | 30 km | 6 km | 1.2 km |
| Vertical Levels | 80 | ” | ” |
| Initial Conditions | 32 km NARR | ” | ” |
| Boundary Conditions | 32 km NARR | ” | ” |
| Start Time | 9 UTC | 12 UTC | 12 UTC |
| End Time | 21 UTC | ” | ” |
| **Physics Settings** | **Domain 1** | **Domain 2** | **Domain 3** |
| Cumulus Convection | Grell-Freitas Ensemble Scheme (3) | None (0) | None (0) |
| Boundary Layer | MYNN 2.5 Level TKE Scheme (5) | ” | ” |
| Surface layer | MYNN Surface Layer (5) | ” | ” |
| Microphysics | Aerosol-Aware Thompson Scheme (28) | ” | ” |
| Land Surface | RUC Land-Surface Model (3) | ” | ” |
| Longwave Radiation | RRTMG Scheme (4) | ” | ” |
| Shortwave Radiation | RRTMG Scheme (4) | ” | ” |

1. The near surface layer (<100 m) was around 1-2°C warmer during the winter precipitation as well as the few hours leading up to it (Fig 3.12A). One hypothesis is that the NARR dataset could have introduced a warm bias at the surface. The NARR has been utilized in several winter weather studies and has been found to have a 1-2 °C warm bias during Oklahoma winter storms (Mullens 2014; Mullens et al. 2016; Mullens and McPherson 2017). Therefore, no refreezing layer was identified by the algorithm discussed in Section 2.3.2.

2. The timing of the event was around 2 hours later in the simulation. Therefore exact time comparisons are not valid for this dataset.

3. The southerly warm air advection was weaker in the WRF, therefore the upper level melting layer was not as pronounced in Fig 3.12A compared to the HRRR melting layer (Fig 3.6).

However, despite the differences in the WRF simulation, this dataset can still be utilized to illustrate what types of measurements can be collected in a winter storm environment on the same temporal scales as UAVs. Three locations were chosen in Oklahoma to provide a variety of environments in the state during this event. Figure 3.13A is located in Stratford, OK (55 km to the southeast of KAEFS) and despite its close proximity to KAEFS, had a warmer melting layer throughout the event in the WRF. Precipitation began at 18:15 UTC and both environments (KAEFS and Stratford) lost the melting layer aloft as the onset of precipiation cooled the environment and the near surface refreezing layer intensified. As precipitation continued at KAEFS, the upper levels of the atmosphere remained below freezing except for a short 15 minutes at 20:15 UTC where a small melting pocket appeared. Conversely, at Stratford, the melting layer quickly redeveloped and by 19:30 UTC, reached its peak thickness extending almost to the surface. The wetbulb profile analyzed by the SBC algorithm classified the KAEFS environment as snow due to the absence of a melting layer (not shown). After 19:15 UTC the classification transitioned to rain/snow due to the lowest 100 m becoming saturated. The Stratford location was classified as rain/snow by 18:30 UTC as this location warmed and reached saturation quicker than KAEFS. However, each of these environments would not have observed any snow or ice accumulations due to the 1-2°C surface temperature.

Figures 3.12A and 3.13A illustrate a high-resolution depiction of the evolution of a winter weather environment that could be captured by UAVs. However, several numerical weather model forecasts and analyses are not operational at these temporal and vertical scales. For example, the HRRR analyses are produced once an hour at a 25 hPa vertical resolution. Figures 3.12B and 3.13B depict the same winter weather environments, but re-sampled at the HRRR temporal and vertical scales.

Figure 3.12B looks similar to the high resolution environment prior to the onset of precipitation at 18:15 UTC. After precipitation begins, small vertical features are not resolved well and the 15 minute melting pocket is not present in the low resolution dataset. In

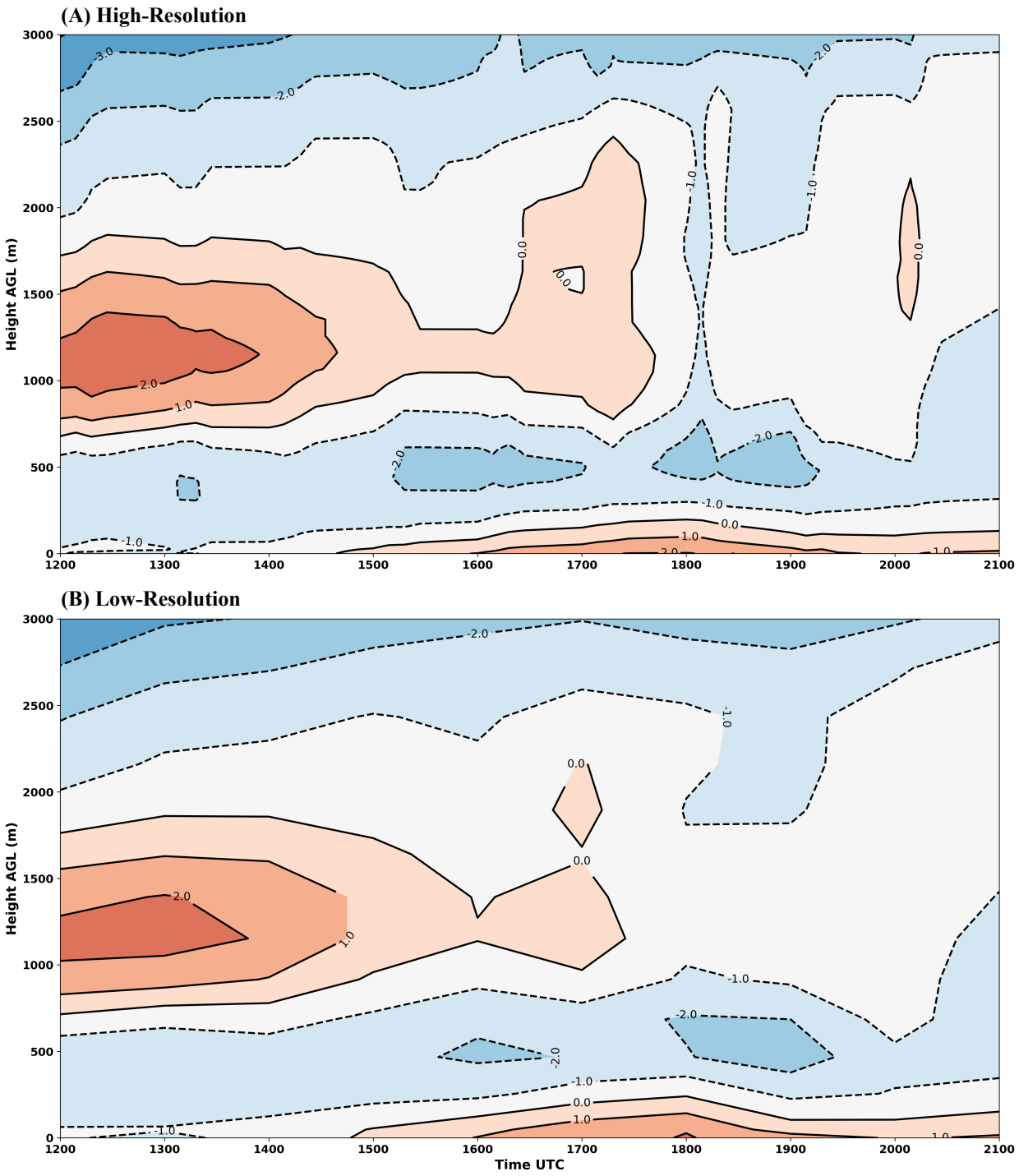


Figure 3.12: 3 km vertical temperature evolution of the WRF atmosphere simulation of February 9th 2019 at KAEFS. (A) Full temporal and vertical resolution. (B) Re-sampled to hourly analyses and 25 hPa vertical resolution. Precipitation began at 18:15 UTC. Solid contours denote values above 0°C and dashed contours are values below 0°C.

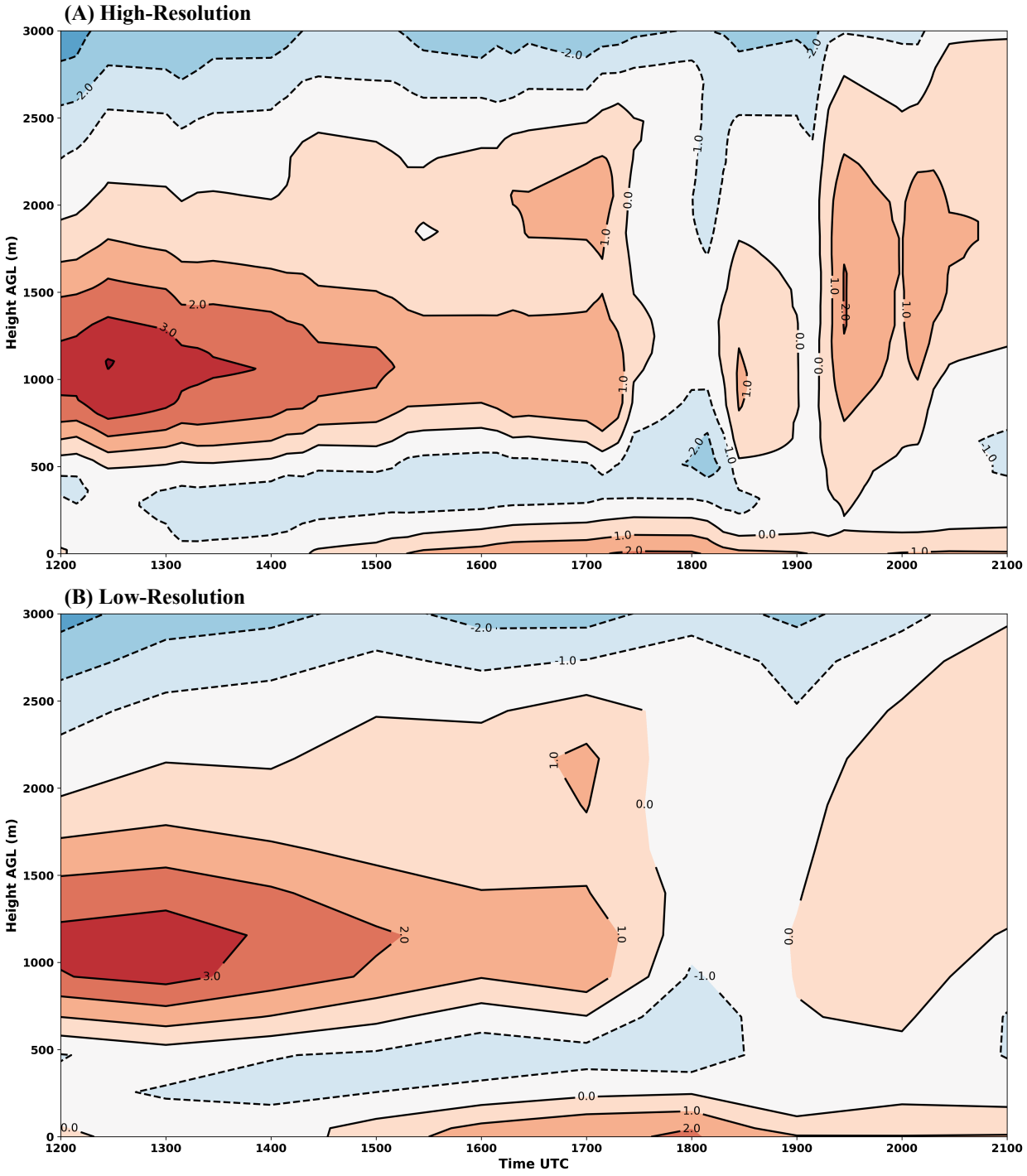


Figure 3.13: 3 km vertical temperature evolution of the WRF atmosphere simulation of February 9th 2019. Same as Figure 3.12, but for Stratford, OK (55 km southeast of KAEFS).

the Stratford environment (Fig. 3.13B), the general structure of the melting and refreezing layers are still discernibly accurate prior to the onset of precipitation. However, once precipitation begins at 18:15 UTC, the temperature in the melting and refreezing layers is not resolved well in the low resolution dataset. Therefore, the SBC algorithm (not shown) favors colder forms of precipitation because of an under-representation of the amount of melting occurring in these layers. This agrees with the findings in Section 3.2.2 that the HRRR may resolve the thickness of melting and refreezing layers well, but struggle to capture the vertical temperature profile at its native vertical and temporal scales.

Farther to the northwest, New Cordell, OK (140 km WNW of KAEFS) was located directly ahead of the surface 0°C isotherm (Fig 3.14). The entire profile was sub-freezing except for the lowest 100 m. Just before precipitation occurred at 18:30 UTC, the upper levels began to warm at 18:15 UTC denoted by the small pocket at -1°C. This quickly diminished and the lower level temperature profile rapidly decreased, reaching close to -5°C from the onset of precipitation. Again, since the surface temperature remained above freezing throughout the precipitation, this environment would see all frozen hydrometeors melt at the surface.

All three of these environments display the evolution of melting and refreezing layers on hourly to sub-hourly temporal scales during active precipitation. These small changes temporally and vertically can have large implications for determining precipitation type from a given vertical profile. Additionally, variability in melting layers separated by 55 km is also evidence of high horizontal variability in environments like this. This further adds to results found in previous studies and this one, that UAV measurements at high temporal and vertical scales, in a statewide mesonet, could provide critical information about melting and refreezing layers across the state.

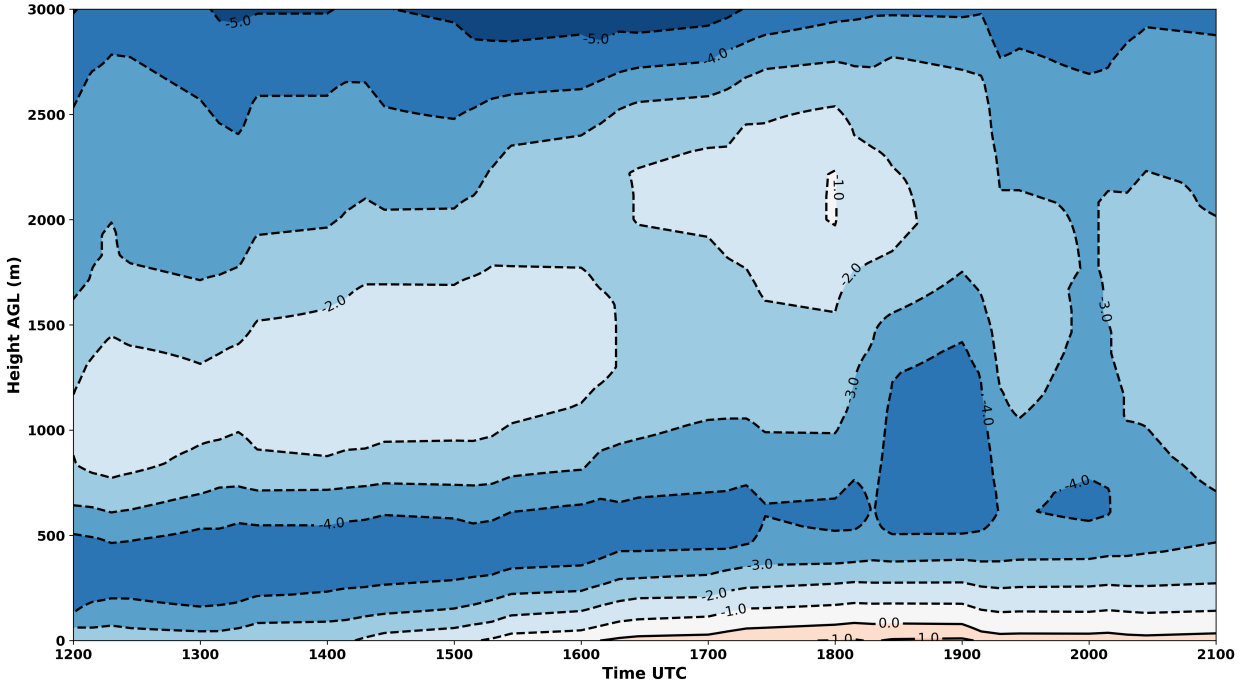


Figure 3.14: 3 km vertical temperature evolution of the WRF atmosphere simulation of February 9th 2019 140 km WNW of KAEFS (New Cordell, OK). Precipitation begin at 18:15 UTC. Solid contours denote values above 0°C and dashed contours are values below 0°C.

# Chapter 4

# Conclusions

**Summary** Oklahoma observes a wide range of winter precipitation types across the state. These hydrometeor types are sensitive to how much melting or refreezing occurs in the lowest 3 km of the atmosphere. Additionally, a change as little as 0.5°C can alter the precipitation type thus presenting a daunting task for numerical weather models. Climatologically, Oklahoma observes more ice storms in the central/southwestern portions of the state and more snow to the northwest. The HRRR 0-hour analyses were utilized to test the accuracy of a 3 km model against observations from UAVs and radiosondes in a winter weather environment measured on February 19, 2019 in central Oklahoma. The HRRR resolved the winter weather environment well in terms of melting and refreezing layer thickness and placement of the surface 0°C isotherm. However, UAV and radiosonde measurements identified a colder refreezing layer (1-2°C) which led to the production of ice pellets. Vertical profiles of wetbulb temperature were analyzed by the SBC algorithm and produced different precipitation classifications between the two datasets. The HRRR analysis wetbulb profile resulted in freezing rain. When UAV data was interpolated into the HRRR analysis, the algorithm output an ice pellet classification which aligned with the observations. An adjustment to the SBC ice nucleation temperature was made to align the output to the precipitation type observations; however, the UAV data correctly identified a 5°C difference in wetbulb temperature from the HRRR. A WRF simulation of the same case study was conducted and produced a similar representation of the winter weather environment with some timing differences. However, when examining a few hypothetical flight locations in Oklahoma, the results illustrate that a horizontal spacing of 55 km could result in different melting/refreezing layer thicknesses and magnitudes. Additionally, the

evolution of the these environments occur on hourly to sub-hourly temporal scales. Comparing the high-resolution WRF dataset to a re-sampled lower resolution version of WRF at these flight locations illustrates that key information for determining precipitation type is lost when employing the native vertical and temporal resolution of the HRRR. Therefore, precise measurements on high temporal, vertical and horizontal scales from UAVs could provide valuable information to models or forecasters.

**Limitations/Constraints/Future Work** This case study represents a small sample of winter weather environments. Therefore, the results herein will not be reflective of every ice pellet environment. Further investigation into the HRRR melting and refreezing layer growth/decay needs to be conducted to explore the efficacy of UAVs in winter weather. Specifically, a study of the temporal evolution of these layers by storm type could provide new insights into how these events unfold.

The authors strongly suggest an extensive study be conducted on icing and other related meteorological conditions that could limit UAV flight performance in winter weather. During the February 19, 2019 case study at KAEFS, the UAV iced several times on the rotors and the shell of the mainframe. However, the aircraft flight performance was not heavily affected during this event. As UAV designs improve, small adjustments to the aircraft could be employed to mitigate icing in critical locations without compromising the measurements. No ice accumulations on the sensor were recorded; however, there were small temperature fluctuations (+0.3°C) noted in the data as the UAV ascended into the upper portions of the flight path. One hypothesis is that brief moments of icing could occur on the sensor causing a quick 0.3°C spike towards 0°C. However, it appeared the ice quickly diminished as the rest of the temperature profile continued decreasing with height, thus moving away from 0°C. Additionally, the rest of the UAV data agreed with other observations in the PBL.

In order for a network of UAVs to gather data across a state, several risk mitigation systems would need to be in place to ensure the safety of the National Airspace System (NAS) controlled by the FAA. Ongoing work outlined in Chilson et al. (2019) describes the utility of the Automatic Dependent Surveillance-Broadcast (ADS-B) system and local air traffic radars for deconflicting the NAS. Incorporating these systems along with an artificial intelligence network for meteorological flight conditions are a few of the necessary steps towards installing this operational network.

Further modeling work should be employed to create an Observation System Simulation Experiment (OSSE). Moore (2018) used this approach to simulate UAV data and then measured the impacts of these measurements when assimilated into models. Specifically, winter weather OSSEs could be created to test the temporal, vertical, and horizontal resolution required to improve winter weather forecasts. Additionally, these data could be utilized to identify the flight ceiling required for different winter weather types, as well as flight constraints expected from a given environment.

This study focused on utilizing UAVs in environments near 0°C due to the importance in small PBL temperature changes. However, cases of extreme winter weather, such as blizzards, lake effect snow or large snow storms were not explored. These environments are strongly driven by synoptic and convective processes on much larger scales. For regions that occasionally observes blizzards, such as the panhandle of Oklahoma, OSSEs could potentially provide insight on if UAV measurements have an impact on forecasts associated with such strong convective and synoptic processes. It is noted that the wind fields associated with these winter weather types pose an extreme challenge for UAV flight performance. This study lays the ground work for future field operations and provides insight on the temporal and horizontal frequency needed for future analyses.

## Bibliography


Alexander, C. R., and Coauthors, 2017: Expanding the High-Resolution Rapid Refresh (HRRR) from Deterministic to Ensemble Data Assimilation, Forecasts and Post-Processing. URL https://ams.confex.com/ams/97Annual/webprogram/Paper309424.html.

Baldwin, M., R. Treadon, and S. Contorno, 1994: Precipitation type prediction using a decision tree approach with nmcs meso- scale eta model. *10th Conf. on Numerical Weather Prediction*, **Portland, OR, Amer. Meteor.Soc., 30-31**.

Barbieri, L., and Coauthors, 2019: Intercomparison of small unmanned aircraft system (suas) measurements for atmospheric science during the lapse-rate campaign. *Sensors*, **19 (9)**, doi:10.3390/s19092179, URL https://www.mdpi.com/1424-8220/19/9/2179.

Bell, T. M., B. R. Greene, P. B. Chilson, P. M. Klein, M. Carney, and D. Turner, 2019: Confronting the boundary layer data gap: Evaluating new and existing methodologies of probing the lower atmosphere. *Atmospheric Measurement Techniques*.

Bourgouin, P., 2000: A method to determine precipitation types. *Weather and Forecasting*, **15 (5)**, 583–592, doi:10.1175/1520-0434(2000)015⟨0583:AMTDPT⟩2.0.CO;2.

Brock, F. V., K. C. Crawford, R. L. Elliott, G. W. Cuperus, S. J. Stadler, H. L. Johnson, and M. D. Eilts, 1995: The Oklahoma Mesonet: A Technical Overview. *Journal of Atmospheric and Oceanic Technology*, **12 (1)**, 5–19, doi:10.1175/1520-0426(1995)012⟨0005:TOMATO⟩2.0.CO;2.

Call, D. A., 2010: Changes in ice storm impacts over time: 1886–2000. *Weather, Climate, and Society*, **2 (1)**, 23–35, doi:10.1175/2009WCAS1013.1.

Changnon, S. A., 2003: Characteristics of ice storms in the united states. *Journal of Applied Meteorology*, **42 (5)**, 630–639, doi:10.1175/1520-0450(2003)042⟨0630:COISIT⟩2.0.CO;2.

Changnon, S. A., D. Changnon, and T. R. Karl, 2006: Temporal and spatial characteristics of snowstorms in the contiguous united states. *Journal of Applied Meteorology and Climatology*, **45 (8)**, 1141–1155, doi:10.1175/JAM2395.1.

Changnon, S. A., and T. R. Karl, 2003: Temporal and spatial variations of freezing rain in the contiguous united states: 1948–2000. *Journal of Applied Meteorology*, **42 (9)**, 1302–1315, doi:10.1175/1520-0450(2003)042⟨1302:TASVOF⟩2.0.CO;2.

Chilson, P. B., and Coauthors, 2019: Moving towards a network of autonomous uas atmospheric profiling stations for observations in the earth's lower atmosphere: The 3d mesonet concept. *Sensors*, **19 (12)**, doi:10.3390/s19122720, URL https://www.mdpi.com/1424-8220/19/12/2720.

Cortinas Jr., J. V., B. C. Bernstein, C. C. Robbins, and J. Walter Strapp, 2004: An analysis of freezing rain, freezing drizzle, and ice pellets across the united states and canada: 1976–90. *Weather and Forecasting*, **19 (2)**, 377–390, doi:10.1175/1520-0434(2004)019⟨0377:AAOFRF⟩2.0.CO;2.

de Boer, G., and Coauthors, 2016: The pilatus unmanned aircraft system for lower atmospheric research. *Atmospheric Measurement Techniques*, **9 (4)**, 1845–1857, doi:10.5194/amt-9-1845-2016, URL https://www.atmos-meas-tech.net/9/1845/2016/.

ESRL, 2016: RAP/HRRR Variable Descriptions. URL https://rapidrefresh.noaa.gov/RAP_var_diagnosis.html, accessed August 2019.

Greene, B. R., A. R. Segales, T. M. Bell, E. A. Pillar-Little, and P. B. Chilson, 2019: Environmental and sensor integration influences on temperature measurements by rotary-wing unmanned aircraft systems. *Sensors*, **19 (6)**, doi:10.3390/s19061470, URL https://www.mdpi.com/1424-8220/19/6/1470.

Greene, B. R., A. R. Segales, S. Waugh, S. Duthoit, and P. B. Chilson, 2018: Considerations for temperature sensor placement on rotary-wing unmanned aircraft systems. *Atmospheric Measurement Techniques*, **11 (10)**, 5519–5530, doi:10.5194/amt-11-5519-2018, URL https://www.atmos-meas-tech.net/11/5519/2018/.

Grout, T., Y. Hong, J. Basara, B. Balasundaram, Z. Kong, and S. T. S. Bukkapatnam, 2012: Significant winter weather events and associated socioeconomic impacts (federal aid expenditures) across oklahoma: 2000–10. *Weather, Climate, and Society*, **4 (1)**, 48–58, doi:10.1175/WCAS-D-11-00057.1.

Horel, B., John; Blaylock, 2018: Archive of the high resolution rapid refresh model. URL http://hrrr.chpc.utah.edu/.

Houston, A. L., B. Argrow, J. Elston, J. Lahowetz, E. W. Frew, and P. C. Kennedy, 2012: The collaborative colorado–nebraska unmanned aircraft system experiment. *Bulletin of the American Meteorological Society*, **93 (1)**, 39–54, doi:10.1175/2011BAMS3073.1.

Ikeda, K., M. Steiner, and G. Thompson, 2017: Examination of mixed-phase precipitation forecasts from the high-resolution rapid refresh model using surface observations and sounding data. *Weather and Forecasting*, **32 (3)**, 949–967, doi:10.1175/WAF-D-16-0171.1, URL https://doi.org/10.1175/WAF-D-16-0171.1.

Koch, S. E., M. Fengler, P. B. Chilson, K. L. Elmore, B. Argrow, D. L. Andra, and T. Lindley, 2018: On the use of unmanned aircraft for sampling mesoscale phenomena in the preconvective boundary layer. *Journal of Atmospheric and Oceanic Technology*, **35 (11)**, 2265–2288, doi:10.1175/JTECH-D-18-0101.1.

McCray, C. D., E. H. Atallah, and J. R. Gyakum, 2019: Long-duration freezing rain events over north america: Regional climatology and thermodynamic evolution. *Weather and Forecasting*, **34 (3)**, 665–681, doi:10.1175/WAF-D-18-0154.1, URL https://doi.org/10.1175/WAF-D-18-0154.1.

McPherson, R. A., and Coauthors, 2007: Statewide Monitoring of the Mesoscale Environment: A Technical Update on the Oklahoma Mesonet. *Journal of Atmospheric and Oceanic Technology*, **24 (3)**, 301–321, doi:10.1175/JTECH1976.1.

Moore, A., 2018: Observing system simulation experiment studies on the use of small uav for boundary-layer sampling. M.S. thesis, University of Oklahoma, Norman, OK, USA.

Mullens, E. D., 2014: Moisture and thermal characteristics of southern plains ice storms: Insights from a regional climatology and high- resolution wrf-arw sensitvity study. Ph.D. thesis, University of Oklahoma, Norman, OK, USA.

Mullens, E. D., L. M. Leslie, and P. J. Lamb, 2016: Synoptic pattern analysis and climatology of ice and snowstorms in the southern great plains, 1993–2011. *Weather and Forecasting*, **31 (4)**, 1109–1136, doi:10.1175/WAF-D-15-0172.1.

Mullens, E. D., and R. McPherson, 2017: A multialgorithm reanalysis-based freezing-precipitation dataset for climate studies in the south-central united states. *Journal of Applied Meteorology and Climatology*, **56 (2)**, 495–517, doi:10.1175/JAMC-D-16-0180.1, URL https://doi.org/10.1175/JAMC-D-16-0180.1.

NARR, 2005: NCEP North American Regional Reanalysis (NARR). Research Data Archive at the National Center for Atmospheric Research, Computational and Information Systems Laboratory, Boulder CO, URL http://rda.ucar.edu/datasets/ds608.0/, accessed January 2019.

NOAA/NCEI, 2014: Storm events database, version 3. NOAA/NCEI, accessed May 2018 to June 2019, https://www.ncdc.noaa.gov/stormevents/.

NRC, 2009: *Observing Weather and Climate from the Ground Up: A Nationwide Network of Networks*. The National Academies Press, Washington, DC, doi:10.17226/12540.

NWS, 2019: WFO Winter Weather Products Specification. URL https://www.nws.noaa.gov/directives/sym/pd01005013curr.pdf, accessed September 2019.

Ralph, F., and Coauthors, 2005: Improving short-term (0 48 h) cool-season quantitative precipitation forecasting: Recommendations from a uswrp workshop. *Bulletin of The American Meteorological Society - BULL AMER METEOROL SOC*, **86**, doi:10.1175/BAMS-86-11-1619.

Ramer, J., 1993: An empirical technique for diagnosing precipitation type from model output. *Fifth Int. Conf. on Aviation Weather Systems*, **Vienna, VA, Amer. Meteor.Soc.**, 227–230.

Rauber, R. M., L. S. Olthoff, M. K. Ramamurthy, D. Miller, and K. E. Kunkel, 2001: A synoptic weather pattern and sounding-based climatology of freezing precipitation in the united states east of the rocky mountains. *Journal of Applied Meteorology*, **40 (10)**, 1724–1747, doi:10.1175/1520-0450(2001)040⟨1724:ASWPAS⟩2.0.CO;2.

Reeves, H. D., 2016: The uncertainty of precipitation-type observations and its effect on the validation of forecast precipitation type. *Weather and Forecasting*, **31 (6)**, 1961–1971, doi:10.1175/WAF-D-16-0068.1.

Reeves, H. D., K. L. Elmore, A. Ryzhkov, T. Schuur, and J. Krause, 2014: Sources of uncertainty in precipitation-type forecasting. *Weather and Forecasting*, **29 (4)**, 936–953, doi:10.1175/WAF-D-14-00007.1.

Reeves, H. D., A. V. Ryzhkov, and J. Krause, 2016: Discrimination between winter precipitation types based on spectral-bin microphysical modeling. *Journal of Applied Meteorology and Climatology*, **55 (8)**, 1747–1761, doi:10.1175/JAMC-D-16-0044.1.

Schuur, T. J., H.-S. Park, A. V. Ryzhkov, and H. D. Reeves, 2012: Classification of precipitation types during transitional winter weather using the ruc model and polarimetric radar retrievals. *Journal of Applied Meteorology and Climatology*, **51 (4)**, 763–779, doi:10.1175/JAMC-D-11-091.1.

Segales, A. R., B. R. Greene, T. M. Bell, W. Doyle, J. J. Martin, E. A. Pillar-Little, and P. B. Chilson, 2019: The coptersonde: An insight into the development of a smart uas for atmospheric boundary layer research. *Atmospheric Measurement Techniques*.

Seidel, D. J., B. Sun, M. Pettey, and A. Reale, 2011: Global radiosonde balloon drift statistics. *Journal of Geophysical Research*, doi:doi.org/10.1029/2010JD014891.

Skamarock, W. C., and Coauthors, 2019: A Description of the Advanced Research WRF Model Version 4. NCAR Tech, URL https://opensky.ucar.edu/islandora/object/technotes:576, (No. NCAR/TN-556+STR), doi:10.5065/1dfh-6p97.

Stewart, R. E., J. M. Thériault, and W. Henson, 2015: On the characteristics of and processes producing winter precipitation types near 0c. *Bulletin of the American Meteorological Society*, **96 (4)**, 623–639, doi:10.1175/BAMS-D-14-00032.1.

Thériault, J. M., R. E. Stewart, and W. Henson, 2010: On the dependence of winter precipitation types on temperature, precipitation rate, and associated features. *Journal of Applied Meteorology and Climatology*, **49 (7)**, 1429–1442, doi:10.1175/2010JAMC2321.1.

UPP, 2019: Unified Post Processor, version 4.0.1. UPP, accessed Sept 2019, https://dtcenter.org/community-code/unified-post-processor-upp.

Waugh, S., and T. J. Schuur, 2018: On the use of radiosondes in freezing precipitation. *Journal of Atmospheric and Oceanic Technology*, **35 (3)**, 459–472, doi:10.1175/JTECH-D-17-0074.1.